J. Fluid Mech. (2003), *vol.* 481, *pp.* 105–148.
DOI: 10.1017/S002211200300380X Printed in the United Kingdom

Inertial and viscous forces on a rigid sphere in straining flows at moderate Reynolds numbers

By PROSENJIT BAGCHI AND S. BALACHANDAR

Department of Theoretical and Applied Mechanics, University of Illinois at Urbana-Champaign, Urbana, IL 61801, USA

(Received 20 March 2001 and in revised form 10 October 2002)

The focus of this paper is the effect of spatial non-uniformity in the ambient flow on the forces acting on a rigid sphere when the sphere Reynolds number, Re, is in the range 10 to 300. Direct numerical simulations (DNS) based on a pseudospectral methodology are carried out to solve for the unsteady three-dimensional flow field around a sphere which is either held stationary or allowed to translate freely under the hydrodynamic forces. The various components of the total force, namely the inertial, steady viscous, and history forces, are systematically estimated in the context of linearly varying straining flows. The inertial forces are isolated by computing the rapid changes in the drag and lift forces in response to a rapid acceleration of the ambient flow. It is shown that the inertial forces arising due to convective acceleration at moderate Reynolds numbers follow the inviscid flow result. While the effect of temporal acceleration depends only on the sign and magnitude of the acceleration, the effect of convective acceleration is shown to depend also on the initial state of the ambient flow. A simple theoretical argument is presented to support the numerical observations. It is also shown that the effect of convective acceleration on the steady viscous force can be realized on a slower time scale. The results show that the history kernels currently available in the literature are not adequate to represent the effect of non-uniformity on the history force.

We isolate the steady viscous force by considering the simulation results for a stationary sphere subjected to steady straining flows. It is shown that the steady viscous forces under such non-uniform ambient conditions cannot be adequately represented by Schiller–Neumann-type drag laws. A generalized representation for the steady viscous force on a sphere subjected to straining flows at moderate Re is presented. The strain-induced corrections to the steady viscous force, under some situations, are shown to be significant and of at least the same order as the inertial forces. In order to further estimate the importance of different forces, we consider direct numerical simulations of the unsteady free translation of a sphere in straining flows. The predictions based on the Schiller–Neumann drag significantly misrepresent the exact force obtained from DNS. The inclusion of the inertial forces improves the prediction when the sphere moves within the same plane of strain, and worsens when the sphere moves away from the plane of strain. The DNS results can be predicted well when the strain-induced corrections to the viscous drag are included. Analysis of the different components of the total force suggests that the Schiller–Neumann drag, the inertial forces due to convective acceleration, and the strain-induced viscous corrections are the dominant components. The contributions from the acceleration of the sphere and the history force are consistently small.

1. Introduction

In the limit of potential flow, the hydrodynamic force exerted on a rigid sphere moving in an unsteady but spatially uniform ambient flow is given by (Lamb 1932; Batchelor 1967)

$$\boldsymbol{F} = m_{\mathrm{f}} \left[\frac{\partial \boldsymbol{U}}{\partial t} + C_M \left(\frac{\partial \boldsymbol{U}}{\partial t} - \frac{\mathrm{d}\boldsymbol{V}}{\mathrm{d}t} \right) \right], \tag{1.1}$$

where $\boldsymbol{U}$ is the undisturbed fluid velocity, $\boldsymbol{V}$ is the velocity of the rigid sphere, m_{f} is the mass of fluid displaced by the sphere and C_M is the added-mass coefficient, which for a sphere is 1/2. The first term on the right-hand side of (1.1) is the effect of the pressure gradient of the ambient flow, and the second term is the added-mass effect due to the temporal acceleration of the fluid and the sphere.

The case of a spatially non-uniform irrotational flow was originally considered by Taylor (1928) and Tollmien (1938). Taylor's inviscid analysis was later revisited and extended by many, including Voinov, Voinov & Petrov (1973), and Auton, Hunt & Prud'homme (1988). For an irrotational ambient flow, Auton *et al.* (1988) showed that the force on a sphere is given by

$$\boldsymbol{F} = m_{\mathrm{f}} \left[\frac{\mathrm{D}\boldsymbol{U}}{\mathrm{D}t} + C_M \left(\frac{\partial \boldsymbol{U}}{\partial t} - \frac{\mathrm{d}\boldsymbol{V}}{\mathrm{d}t} \right) + C_M \boldsymbol{U} \cdot \nabla \boldsymbol{U} \right]. \tag{1.2}$$

Here $\mathrm{D}/\mathrm{D}t = \partial/\partial t + \boldsymbol{U} \cdot \nabla$ is the total derivative following the local fluid element. The first two terms on the right are similar to those in (1.1) representing the pressure gradient and the added-mass forces. The last term represents the added-mass force due to spatial non-uniformity in the undisturbed flow. In (1.2), $\boldsymbol{U}$ and its derivatives are computed at the instantaneous location of the centre of the sphere.

On the other hand, in the limit of Stokes flow, i.e. as the sphere Reynolds number $Re = |\boldsymbol{U} - \boldsymbol{V}|d/\nu \to 0$, the unsteady motion of the sphere moving in an otherwise stagnant fluid is given by the classical Basset–Boussinesq–Oseen (BBO) equation. A generalization to the BBO equation for a non-uniform flow was first proposed by Tchen (1947). Several subsequent works have corrected and improved upon the results of Tchen. The final form was obtained by Maxey & Riley (1983) and by Gatignol (1983) as

$$\boldsymbol{F} = 3\pi\mu d(\boldsymbol{U} - \boldsymbol{V}) + \frac{3}{2} d^2 \sqrt{\pi \rho_{\mathrm{f}} \mu} \int_0^t \frac{\mathrm{d}\boldsymbol{U}/\mathrm{d}\tau - \mathrm{d}\boldsymbol{V}/\mathrm{d}\tau}{\sqrt{t - \tau}} \, \mathrm{d}\tau + m_{\mathrm{f}} \left[\frac{\mathrm{D}\boldsymbol{U}}{\mathrm{D}t} + C_M \left(\frac{\mathrm{d}\boldsymbol{U}}{\mathrm{d}t} - \frac{\mathrm{d}\boldsymbol{V}}{\mathrm{d}t} \right) \right]. \tag{1.3}$$

Here d is the diameter of the sphere, ρ_{f} and μ are the density and viscosity of the fluid, and $\mathrm{d}/\mathrm{d}t = \partial/\partial t + \boldsymbol{V} \cdot \nabla$ is the total derivative following the sphere. There are two additional terms arising from the viscous effects: the first term on the right-hand side is the Stokes drag, and the second term is the Basset history force. Faxén corrections that account for the quadratic variation in the fluid velocity are ignored here.

In many practical situations, however, the sphere Reynolds number is moderate ($1 < Re < 10^3$) and the extension of the theoretical results from the inviscid and creeping flow limits to moderate Re is not straightforward. Motivated by the inviscid and creeping flow results, the extension to moderate Re can be expressed as (Magnaudet & Eames 2000)

$$\boldsymbol{F} = \boldsymbol{F}_{\rm sv} + 3d\pi\mu \int_{-\infty}^{t} K(t,\tau)\left(\frac{\mathrm{d}\boldsymbol{U}}{\mathrm{d}\tau} - \frac{\mathrm{d}\boldsymbol{V}}{\mathrm{d}\tau}\right)\mathrm{d}\tau + m_{\rm f}\left[\frac{\mathrm{D}\boldsymbol{U}}{\mathrm{D}t} + \mathrm{C_M}\left(\frac{\partial \boldsymbol{U}}{\partial t} - \frac{\mathrm{d}\boldsymbol{V}}{\mathrm{d}t}\right) + C_M \boldsymbol{U}\cdot\nabla\boldsymbol{U}\right]. \quad (1.4)$$

The justification of such a representation requires precise definitions of the different terms based on physical mechanisms. The first two terms are viscous (non-inertial) in origin, while the remaining terms are inertial. The inertial forces are realized on a rapid time scale, while the non-inertial forces develop on a slow diffusion time scale. The inertial forces can be further separated into contributions from the pressure gradient and the added-mass forces. The non-inertial effect can be separated into a steady and a transient component. The steady viscous force, $\boldsymbol{F}_{\rm sv}$, is defined to be dependent only on the local instantaneous state of the fluid and sphere (i.e. only on $\boldsymbol{U}-\boldsymbol{V}$ and $\nabla\boldsymbol{U}$). The transient component is similar to the Basset force whose kernel $K(t,\tau)$ decays as $(t-\tau)^{-1/2}$ for a short time and much quicker over a longer time. Under steady conditions in a uniform ambient flow the history force becomes zero and $\boldsymbol{F}_{\rm sv}$ reduces to the so-called 'standard drag'.

It is a common practice in the Lagrangian tracking of particles in multiphase flow studies to simply use empirical drag laws, such as the popular one given by Schiller & Neumann (1933),

$$\boldsymbol{F} \approx \boldsymbol{F}_{\rm sv} \approx 3\pi\mu d(\boldsymbol{U}-\boldsymbol{V})[1+0.15\,Re^{0.687}]. \quad (1.5)$$

The effect of temporal and spatial gradients as represented by the history and added-mass forces is ignored in such simple drag laws. The effect of $\nabla\boldsymbol{U}$ on $\boldsymbol{F}_{\rm sv}$ is also ignored. The above force law is well justified under steady conditions in a uniform flow. However, its widespread usage despite this is due to a lack of complete confidence in more complex force representations, such as the one given in (1.4). As pointed out by Magnaudet (1997), our understanding needs to improve along three different fronts: (i) the added-mass force must be firmly established in non-uniform ambient flows, (ii) the steady viscous drag, $\boldsymbol{F}_{\rm sv}$, must be generalized to non-uniform ambient flows by considering its dependence on $\nabla\boldsymbol{U}$, and (iii) a generalization of the history force in non-uniform flows must be sought. The primary focus of this paper is to improve our understanding of the above three issues. Attention will be limited to irrotational ambient flows: thus we will avoid any discussion of the rotational lift force or the effect of ambient vorticity on the steady viscous drag.

1.1. *Added-mass force*

The past decade has seen several significant contributions towards an improved understanding of the added-mass force (Rivero, Magnaudet & Fabre 1991; Chang & Maxey 1995; Mei, Lawrence & Adrian 1991; Howe 1995; Mougin & Magnaudet 2001; also see Magnaudet & Eames 2000). The focus has generally been on the added-mass force at moderate Re arising from the temporal acceleration of either the fluid or the sphere, or both. Mei *et al.* (1991) computed the unsteady force on a stationary sphere in an oscillatory flow and extracted the added-mass force from the imaginary part of the unsteady drag in the high-frequency limit. They deduced that the added-mass coefficient for temporal acceleration at moderate Re was the same as that in the creeping and potential flow limits. Rivero *et al.* (1991) used a clever numerical procedure to separate the history and added-mass forces from the total unsteady force. Their investigations of oscillatory and uniformly accelerating flows

established the inviscid result of $C_M = 1/2$ to be valid even at moderate Re. Chang & Maxey (1995) exploited the fact that in an accelerating flow the inertial forces are immediately realized after the application of the acceleration, while the viscous effects grow on a slower time scale. By considering the forces on a sphere subjected to temporally accelerating and decelerating uniform flows ($\nabla \boldsymbol{U} = 0$, $\partial \boldsymbol{U}/\partial t \neq 0$) and by examining the time evolution of the drag force over a short time, they confirmed $C_M = 1/2$ to be valid at moderate Re. More recently Howe (1995) and Mougin & Magnaudet (2001) have shown more rigorously that the concept of the added-mass is well-defined at moderate Re in the presence of both free and surface-generated vorticity.

While the added-mass force due to temporal acceleration has received much attention, that due to convective acceleration of the fluid is relatively less studied. As pointed out by Magnaudet, Rivero & Fabre (1995), in non-uniform flows, the separation of the added-mass force is complicated by the fact that the non-uniformity not only induces an inertial force but also modifies the viscous drag as a direct consequence of the changes in the surface vorticity distribution. They performed simulations of straining ambient flows over a solid sphere and a spherical bubble at moderate Re. Based on the computed pressure drag, they evaluated the added-mass coefficient for convective acceleration to be $1/2$. Here we consider an approach similar to that taken by Rivero *et al.* (1991) and Chang & Maxey (1995) for the case of temporal acceleration, and extend that approach to isolate the inertial forces in the presence of convective acceleration. We consider simulations of rapidly imposed straining flows on a stationary sphere. By monitoring the time evolution of the drag and lift forces over a short time we isolate the added-mass force. The present results therefore add to our current understanding of the added-mass force in non-uniform flows.

1.2. *Effect of strain on* $\boldsymbol{F}_{\mathrm{sv}}$

In a non-uniform ambient flow the steady viscous force $\boldsymbol{F}_{\mathrm{sv}}$ is modified as a direct result of the changes in the surface distribution of vorticity and pressure. In axisymmetric straining flows, Magnaudet *et al.* (1995) have shown a substantial increase in the viscous drag over that of the corresponding uniform flow. In planar straining flows, and for straining flows oriented at an angle to the relative velocity, Bagchi & Balachandar (2002*a*) observed an even larger influence on the drag and lift forces. It thus appears that in the presence of ambient flow inhomogeneity, $\boldsymbol{F}_{\mathrm{sv}}$ may no longer be adequately represented by drag laws of the form (1.5). In addition to the dependence of $\boldsymbol{F}_{\mathrm{sv}}$ on local relative velocity $|\boldsymbol{U} - \boldsymbol{V}|$, the effect of $\nabla \boldsymbol{U}$ must also be included. Using direct numerical simulation results for axisymmetric straining flows (Magnaudet *et al.* 1995) and planar straining flows (Bagchi & Balachandar 2002*a*) past a stationary sphere, we isolate the steady viscous contribution. The results are shown to be substantially different from the Schiller–Neumann formula (1.5). A parameterization for $\boldsymbol{F}_{\mathrm{sv}}$ in terms of $|\boldsymbol{U} - \boldsymbol{V}|$ and $\nabla \boldsymbol{U}$ is then presented for selected orientations of the axisymmetric and planar straining flows. The strain-induced viscous corrections to $\boldsymbol{F}_{\mathrm{sv}}$ are shown to be of the order of the inertial forces, under some orientations of the ambient strain.

We further examine the effect of non-uniformity by performing a direct numerical simulation (DNS) of a freely translating sphere in straining flow, where the sphere is moved in response to the drag and lift forces computed from the surface distribution of the pressure and shear stress. The results show that the Schiller–Neumann law (1.5) can significantly mispredict the exact force. Inclusion of the inertial forces can

improve the prediction. However, in some cases further inclusion of the strain-induced corrections to $\boldsymbol{F}_{sv}$ is needed for satisfactory prediction of the DNS results. These test cases validate the parameterization of $\boldsymbol{F}_{sv}$ proposed in this paper for straining flows.

1.3. *History force in non-uniform flows*

The precise form of the history kernel at finite Re is not fully settled even in a uniform ambient flow. It is generally accepted that the history kernel, K in (1.4), varies as $(t-\tau)^{-1/2}$ for short times, and as $(t-\tau)^{-2}$ for longer times (Mei *et al.* 1991; Mei & Adrian 1992; Lovalenti & Brady 1993; Kim, Elghobashi & Sirignano 1998). The representation is likely to be more complex in a non-uniform ambient flow. Magnaudet *et al.* (1995) have shown that a naive introduction of the convective acceleration using $\mathrm{D}\boldsymbol{U}/\mathrm{D}t$ in the history integral can lead to erroneous results. In the present work, further insight into the history force is obtained on two fronts. First, the moderate-Re history kernel of the form obtained by Mei & Adrian (1992), which works well for the case of an unsteady uniform flow, is shown to be inadequate for the case of convective acceleration. It is shown that when a straining flow is rapidly imposed on a viscously developed flow, the short-time effects of the inertial forces are masked by the history force, whose magnitude can be very high. Second, from the DNS results of the freely translating sphere in straining ambient flows, we extract the history force during the unsteady motion of the sphere. The results suggest that for the case of free translation under ambient straining flow the history force is not significant.

In the following section, the numerical methodology used in the present study is described. Section 3 presents the results on rapid acceleration of the ambient flow to isolate the inertial forces. The estimation of $\boldsymbol{F}_{sv}$ and its generalized representation are given in §§4 and 5. Finally, the unsteady results corresponding to a freely translating sphere are presented in §6.

2. Problem formulation

2.1. *Governing equations*

We consider the unsteady, three-dimensional flow generated by a rigid sphere moving in a linearly varying ambient flow. With respect to a fixed reference frame $(\boldsymbol{X}, \tau)$, the ambient flow is prescribed as

$$\boldsymbol{U} = U\boldsymbol{e}_X + \boldsymbol{X}\cdot(\boldsymbol{S}+\boldsymbol{\Omega}), \tag{2.1}$$

where U is the oncoming uniform component. Without loss of generality, U is assumed to be directed along the positive X-axis. $\boldsymbol{S}$ and $\boldsymbol{\Omega}$ are the pure straining and rotational components of the velocity gradient $\nabla\boldsymbol{U}$. In general, U, $\boldsymbol{S}$ and $\boldsymbol{\Omega}$ are time-dependent in the case of an unsteady ambient flow. For brevity, in this paper we will consider irrotational ambient flows only ($\boldsymbol{\Omega}=\boldsymbol{0}$). The formulation and methodology described below are applicable to rotational flows as well.

The strain tensor $\boldsymbol{S}$ is characterized in terms of its eigenvalues σ_1, σ_2 and σ_3 ($|\sigma_1| > |\sigma_2| > |\sigma_3|$). In an incompressible flow the sum of the eigenvalues is constrained to be zero and the largest two eigenvalues are of opposite sign. Their ratio $f_s = |\sigma_2|/|\sigma_1|$ is bounded by $1/2 \leqslant f_s \leqslant 1$, where $f_s = 1/2$ implies axisymmetric strain and $f_s = 1$ implies planar strain. For a general case when the principal axes of $\boldsymbol{S}$ are at an angle to the coordinate axes (X, Y or Z), the orientation of the strain-rate tensor needs to be defined as well. The angles Θ and Φ describe the orientation of $\boldsymbol{S}$ with respect to the relative velocity $\boldsymbol{U}_r = \boldsymbol{U}(\boldsymbol{X}_p) - \boldsymbol{V}$, where $\boldsymbol{X}_p$ is the instantaneous position of the

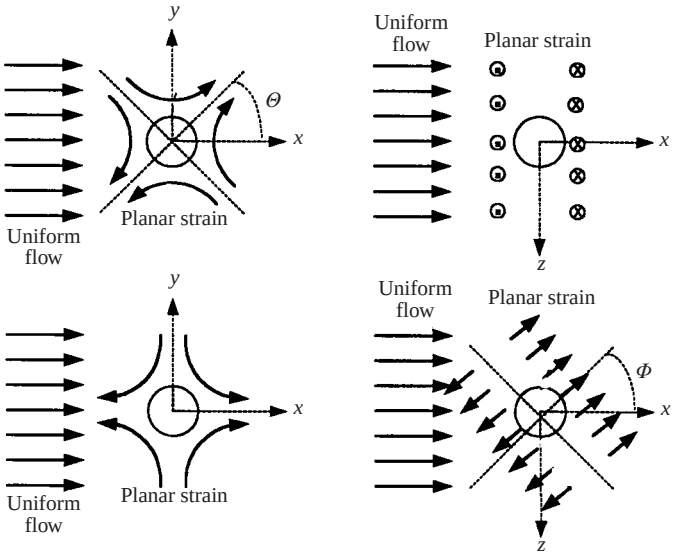

FIGURE 1. Strain configuration with respect to the uniform component of the ambient flow. Θ represents the in-plane orientation of the converging direction of the strain tensor with the uniform flow, while Φ represents the out-of-plane orientation.

centre of the sphere. Θ is the angle between $\boldsymbol{U}_r$ and the principal direction associated with σ_1. Φ is the angle between $\boldsymbol{U}_r$ and the plane formed by the the principal directions associated with σ_1 and σ_2 (see figure 1). Therefore the four parameters that fully characterize the instantaneous strain rate are the largest eigenvalue ($\sigma = \sigma_1$), the nature of the strain (f_s) and the orientation (Θ and Φ). For axisymmetric strain, results will be independent of Φ.

The presence of the sphere introduces a disturbance field $\boldsymbol{U}'(\boldsymbol{X}, \tau)$. The resultant flow field is then given by $\boldsymbol{U} + \boldsymbol{U}'$. At a large distance from the sphere, $\boldsymbol{U}'$ approaches zero. On the surface of the sphere, the no-slip and no-penetration conditions require that $\boldsymbol{U}' = \boldsymbol{V} - \boldsymbol{U}(\boldsymbol{X}_p + (d/2)\boldsymbol{e}_r)$. The resultant flow field satisfies the incompressibility condition and the Navier–Stokes equation. In terms of $\boldsymbol{U}'$, the governing equations in dimensional form are written as

$$\nabla \cdot \boldsymbol{U}' = \boldsymbol{0}, \tag{2.2}$$

$$\frac{\partial \boldsymbol{U}'}{\partial \tau} + \boldsymbol{U}' \cdot \nabla \boldsymbol{U}' + \boldsymbol{U}' \cdot \nabla \boldsymbol{U} + \boldsymbol{U} \cdot \nabla \boldsymbol{U}' = -\frac{1}{\rho_{\mathrm{f}}} \nabla p' + \nu \nabla^2 \boldsymbol{U}'. \tag{2.3}$$

Here the resultant pressure is written as $P + p'$, and P is related to $\boldsymbol{U}$ by

$$-\frac{1}{\rho_{\mathrm{f}}} \nabla P = \frac{\partial \boldsymbol{U}}{\partial \tau} + \boldsymbol{U} \cdot \nabla \boldsymbol{U}. \tag{2.4}$$

We introduce a non-inertial reference frame $(\boldsymbol{x}, t)$ which moves with the sphere and with origin located at the centre of the sphere. In the non-inertial frame, using the transformation

$$\boldsymbol{u}(\boldsymbol{x}, t) = \boldsymbol{U}'(\boldsymbol{X}, \tau) - \boldsymbol{V}(\tau), \tag{2.5}$$

(2.2) and (2.3) can be written as

$$\nabla \cdot \boldsymbol{u} = \boldsymbol{0}, \tag{2.6}$$

$$\frac{\partial \boldsymbol{u}}{\partial t} + \frac{\mathrm{d}\boldsymbol{V}}{\mathrm{d}t} + \boldsymbol{u}\cdot\nabla\boldsymbol{u} + \boldsymbol{U}\cdot\nabla\boldsymbol{u} + \boldsymbol{u}\cdot\nabla\boldsymbol{U} + \boldsymbol{V}\cdot\nabla\boldsymbol{U} = -\frac{1}{\rho_{\mathrm{f}}}\nabla p' + \nu\nabla^2\boldsymbol{u}. \tag{2.7}$$

At a distance far from the sphere, $\boldsymbol{u}$ satisfies the condition $\boldsymbol{u} = -\boldsymbol{V}$. On the surface of the sphere, it satisfies $\boldsymbol{u} = -\boldsymbol{U}(\boldsymbol{X}_p + (d/2)\boldsymbol{e}_r)$. The equations are made dimensionless with appropriate reference variables which are described in a later section. The sphere Reynolds number is defined as $Re = d|\boldsymbol{U}_r|/\nu$, and the dimensionless strain magnitude is defined as $s = \sigma d/|\boldsymbol{U}_r|$.

The resultant force (in dimensional form) on the sphere is obtained by integrating the normal and tangential stresses on the surface:

$$F_i = \int_S \left[-(p' + P)\,\boldsymbol{e}_r + \tau_{r\theta}\,\boldsymbol{e}_\theta + \tau_{r\phi}\,\boldsymbol{e}_\phi\right]\cdot\boldsymbol{e}_i\,\mathrm{d}S, \tag{2.8}$$

where $\tau_{r\theta}$ and $\tau_{r\phi}$ are computed from the net velocity field. The first term on the right-hand side is the pressure force, while the next two terms are the viscous force. A non-dimensional force coefficient is defined as

$$\boldsymbol{C}_{\boldsymbol{F}} = \frac{\boldsymbol{F}}{\frac{1}{2}\rho_{\mathrm{f}}|\boldsymbol{U}_r|^2\,\pi(d/2)^2}. \tag{2.9}$$

The component of $\boldsymbol{C}_{\boldsymbol{F}}$ along $\boldsymbol{U}_r$ is the drag coefficient C_D. Due to the three-dimensional nature of the flow, a lift force normal to $\boldsymbol{U}_r$ may also be generated which will be characterized by a lift coefficient C_L.

In addition to solving the fluid flow equations, the sphere is advected by

$$\boldsymbol{F} + \boldsymbol{F}_{\mathrm{ext}} = m_p\boldsymbol{a}_p, \qquad \frac{\mathrm{d}\boldsymbol{V}}{\mathrm{d}\tau} = \boldsymbol{a}_p, \qquad \frac{\mathrm{d}\boldsymbol{X}_p}{\mathrm{d}\tau} = \boldsymbol{V}, \tag{2.10}$$

where m_p is the mass of the sphere and $\boldsymbol{a}_p$ is its acceleration. $\boldsymbol{F}_{\mathrm{ext}}$ is an externally applied force and it is equal to $-\boldsymbol{F}$ for a stationary sphere and zero for a freely moving sphere.

2.2. *Numerical methods*

The governing equations are solved in a spherical coordinate system (r, θ, ϕ) where

$$d/2 \leqslant r \leqslant R, \qquad 0 \leqslant \theta \leqslant \pi, \qquad 0 \leqslant \phi \leqslant 2\pi.$$

Here R represents the boundary of the computational domain. A pseudospectral (collocation) method is used to solve the unsteady three-dimensional equations. The method is described in greater detail in Bagchi & Balachandar (2000*a*). In brief, a Chebyshev collocation scheme is used in the radial direction while a Fourier collocation is used in the azimuthal (ϕ) direction. In the tangential direction (θ), appropriate expansions for the flow variables are obtained by satisfying the 'pole parity' conditions. Such conditions arise due to the fact that the tangential and azimuthal components of a vector and its derivatives change sign over the poles at $\theta = 0$ and π. The expansion functions depend on the odd or even mode of the azimuthal wavenumber k and are given by

$$u_r = \begin{cases} \sum \cos m\theta & \text{even} \quad k \\ \sum \sin m\theta & \text{odd} \quad k, \end{cases} \tag{2.11}$$

$$u_\theta, u_\phi = \begin{cases} \sum \sin m\theta & \text{even} \quad k \\ \sum \cos m\theta & \text{odd} \quad k. \end{cases} \tag{2.12}$$

A typical grid used in the simulation has 81, 80 and 32 points in the radial, tangential and azimuthal directions, respectively. A grid stretching is used to cluster grid points near the surface of the sphere and in the wake region.

A two-step time-split scheme is used to advance the flow field from time level 'n' to '$n+1$':

$$\text{advection–diffusion} \quad \text{step}: \qquad \frac{\boldsymbol{u}_\star - \boldsymbol{u}_n}{\Delta t} + \boldsymbol{NL}(\boldsymbol{u}_n) = \nu\, \boldsymbol{D}(\boldsymbol{u}_\star), \tag{2.13}$$

$$\text{pressure–correction} \quad \text{step}: \qquad \frac{\boldsymbol{u}_{n+1} - \boldsymbol{u}_\star}{\Delta t} = -\frac{1}{\rho_{\mathrm{f}}} \nabla p'_{n+1}, \tag{2.14}$$

where $\boldsymbol{D}$ and $\boldsymbol{NL}$ are the diffusion and nonlinear terms. The nonlinear terms are treated explicitly using a second-order Adams–Bashforth scheme while the diffusion terms are treated implicitly using a Crank–Nicolson scheme. Pressure at '$n+1$' is obtained by solving a Poisson equation

$$\frac{1}{\rho_{\mathrm{f}}} \nabla^2 p'_{n+1} = \frac{\nabla \cdot \boldsymbol{u}_\star}{\Delta t}. \tag{2.15}$$

The implicit treatment of the above equation satisfies the divergence-free condition, $\nabla \cdot \boldsymbol{u}_{n+1} = \boldsymbol{0}$.

At the inflow boundary, a Dirichlet boundary condition specifying the ambient flow is used. At the outflow, a non-reflecting boundary condition from Mittal & Balachandar (1996) is used. On the surface of the sphere, no-slip and no-penetration conditions are implemented as

$$\boldsymbol{u}_\star = -\boldsymbol{U}(\boldsymbol{X}_p) + \frac{1}{\rho_{\mathrm{f}}} \Delta t (2\nabla p'_n - \nabla p'_{n-1}). \tag{2.16}$$

Combined with a homogeneous Neumann boundary condition for pressure,

$$\partial p'_{n+1}/\partial r = 0, \tag{2.17}$$

(2.16) guarantees zero penetration through the surface of the sphere, while the no-slip condition is satisfied to $O(\Delta t^3)$. A typical non-dimensional time-step used in the present study is $\Delta t |\boldsymbol{U} - \boldsymbol{V}|/d = 0.001$. In simulations of rapid acceleration of the ambient flow, the time-step is further reduced.

3. Rapidly accelerating flows

In this section we compute the inertial forces (added-mass and pressure gradient forces) due to convective acceleration of the ambient flow. The sphere is held stationary and its centre coincides with the origin of the fixed frame ($\boldsymbol{X}$). The flow is accelerated rapidly either from a stagnant condition or from a fully (viscously) developed initially steady condition. As the flow accelerates, the no-slip condition on the surface of the sphere results in the generation of vorticity, which diffuses out radially at the diffusion time scale and then advects downstream at the convective time scale. For a short period of time after the initiation of acceleration, vorticity has very little time to diffuse away from the surface and remains confined to a thin region. Away from this region, the flow can be assumed to be nearly potential. In contrast, the inviscid effect of no penetration through the surface is instantaneously realized and appears as the added-mass and pressure gradient forces. Thus, on a short time scale any changes in the drag and lift forces should be given by the inviscid flow result (1.2).

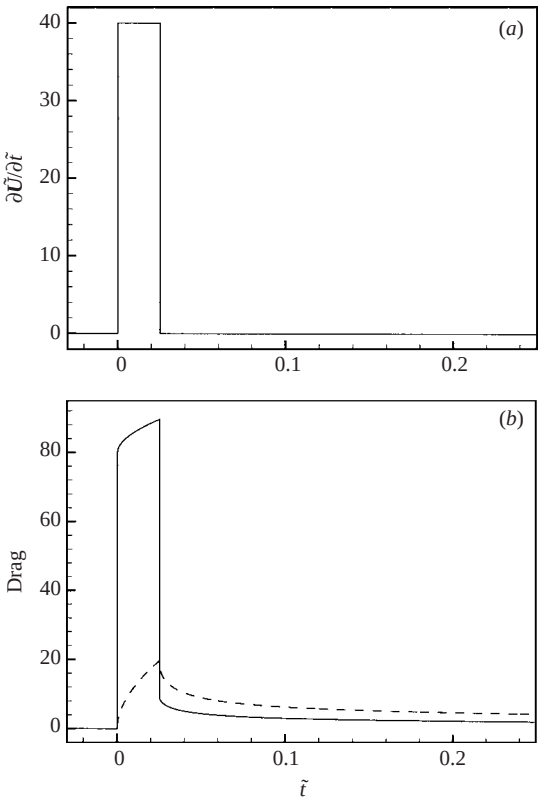

FIGURE 2. (*a*) Temporal acceleration of the free stream and (*b*) the drag coefficient with time: ——, C_{PD}; - - - - - -, C_{VD}.

This idea was originally employed by Rivero *et al.* (1991) and Chang & Maxey (1995) for unsteady but uniform ambient flows. In the following subsection, we first reproduce their results for temporal acceleration to validate our simulation technique. We then extend the methodology to the case of convective acceleration.

3.1. *Effect of temporal acceleration*

We begin with a case where the fluid around the sphere is stagnant for $t \leqslant 0$. For $0 \leqslant t \leqslant t_0$, the ambient flow is linearly accelerated to a new velocity $U_0\boldsymbol{e}_X$. To non-dimensionalize the variables, we use the sphere diameter d as the reference length scale, U_0 as the velocity scale, and d/U_0 as the reference time scale. Dimensionless variables are denoted by a tilde. Then, the ambient flow is given by

$$\left.\begin{aligned} \tilde{\boldsymbol{U}}(\tilde{t}) &= 0, \quad \tilde{t} \leqslant 0, \\ \tilde{\boldsymbol{U}}(\tilde{t}) &= \frac{\tilde{t}}{\tilde{t}_0}\,\boldsymbol{e}_X, \quad 0 \leqslant \tilde{t} \leqslant \tilde{t}_0, \\ \tilde{\boldsymbol{U}}(\tilde{t}) &= \boldsymbol{e}_X, \quad \tilde{t} \geqslant \tilde{t}_0. \end{aligned}\right\} \tag{3.1}$$

Hence the magnitude of the acceleration is given by $1/\tilde{t}_0$ and is maintained constant over $0 \leqslant \tilde{t} \leqslant \tilde{t}_0$ (see figure 2*a*). For a short period after the initiation of acceleration the drag force should be approximated well by the inviscid flow result. Then, using

(1.2) in dimensionless form, the drag coefficient can be written as

$$C_D = \tfrac{4}{3}(1 + C_M)\frac{\partial \tilde{\boldsymbol{U}}}{\partial \tilde{t}}. \tag{3.2}$$

Figure 2(*b*) shows the time variation in the pressure (C_{PD}) and viscous (C_{VD}) components of the drag coefficient for $1/\tilde{t}_0 = 40$. Over a short period of time, of the order of a time step $\Delta\tilde{t} = 10^{-4}$, the only change observed is in the pressure drag, in the form of a sudden change of about 80 at $\tilde{t} = 0$. By (3.2), the drag coefficient due to the added-mass and pressure gradient effects becomes $\frac{160}{3}(1 + C_M)$. Thus, the change in C_{PD} of about 80 corresponds to $C_M = 1/2$. At the end of the acceleration ($\tilde{t} = 0.025$), the pressure drag suffers a sudden drop and the magnitude of this change is again approximately equal to 80, consistent with the inviscid flow prediction. Subsequently, C_{PD} and C_{VD} approach their steady-state values corresponding to $Re = dU_0/\nu = 10$. The simulation reproduces the results of Rivero *et al.* (1991) and Chang & Maxey (1995). It also confirms that the numerical methodology adopted here works well for the case of rapidly accelerated flows.

3.2. *Effect of convective acceleration*

Now we examine the influence of rapidly imposed straining flows. The sphere is held stationary and for $t \leqslant 0$ the fluid around it is stagnant. For $0 \leqslant t \leqslant t_0$, a straining flow is imposed on the sphere along with a temporally accelerating uniform flow. At $t = t_0$, the uniform component reaches $U_0\boldsymbol{e}_X$ and the strain-rate tensor reaches $\boldsymbol{S}_0$. At this point the temporal acceleration of the uniform flow is stopped and the imposed strain-rate is maintained at $\boldsymbol{S}_0$ for $t \geqslant t_0$. Hence, the ambient flow in dimensionless form is given by

$$\left.\begin{aligned} \tilde{\boldsymbol{U}}(\tilde{t}) &= 0, \quad \tilde{t} \leqslant 0, \\ \tilde{\boldsymbol{U}}(\tilde{t}) &= \frac{\tilde{t}}{\tilde{t}_0}\,\boldsymbol{e}_X + \tilde{\boldsymbol{X}} \cdot \tilde{\boldsymbol{S}}(\tilde{t}), \quad 0 \leqslant \tilde{t} \leqslant \tilde{t}_0, \\ \tilde{\boldsymbol{U}}(\tilde{t}) &= \boldsymbol{e}_X + \tilde{\boldsymbol{X}} \cdot \tilde{\boldsymbol{S}}_0, \quad \tilde{t} \geqslant \tilde{t}_0. \end{aligned}\right\} \tag{3.3}$$

Figure 3(*a*) shows the time history of temporal acceleration, $\partial\tilde{\boldsymbol{U}}/\partial\tilde{t}$, measured at the centre of the sphere ($\tilde{\boldsymbol{X}} = 0$), and the non-dimensional strain magnitude, $s = \sigma d/U_0$. As in the previous case, the temporal acceleration is chosen to be $1/\tilde{t}_0 = 40$. The final Reynolds number at the end of acceleration is 10. The strain rate is axisymmetric in nature and its elongational direction is aligned with the X-axis so that

$$\tilde{\boldsymbol{S}} = \begin{bmatrix} s & 0 & 0 \\ 0 & -s/2 & 0 \\ 0 & 0 & -s/2 \end{bmatrix}. \tag{3.4}$$

At $\tilde{t} = 0.025$, the strain magnitude s reaches a value of $s_0 = 0.2$. In the absence of strain, the example considered here is the same as in the previous case (§ 3.1 and figure 2*b*) and the drag coefficient is given by (3.2). When $\tilde{\boldsymbol{S}} \neq 0$, (1.2) in non-dimensional form becomes

$$C_D = \tfrac{4}{3}(1 + C_M)\frac{\partial \tilde{\boldsymbol{U}}}{\partial \tilde{t}} + \tfrac{4}{3}(1 + C_M)\frac{\tilde{t}}{\tilde{t}_0}s. \tag{3.5}$$

Thus, the addition of strain, according to the inviscid theory (1.2), further enhances the drag coefficient by

$$\tfrac{4}{3}(1 + C_M)s\tilde{t}/\tilde{t}_0 \quad \text{for} \quad 0 \leqslant \tilde{t} \leqslant \tilde{t}_0, \qquad \text{and} \quad \tfrac{4}{3}(1 + C_M)s_0 \quad \text{for} \quad \tilde{t} \geqslant \tilde{t}_0,$$

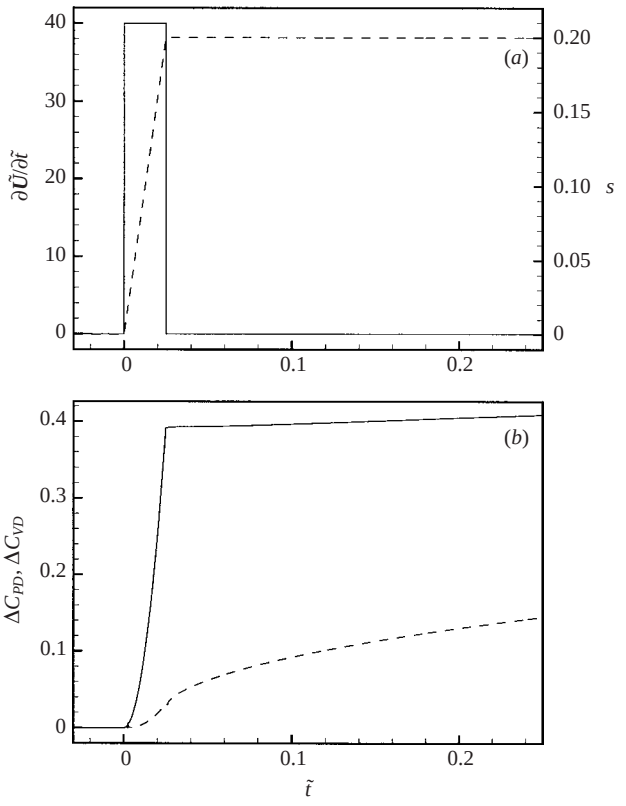

FIGURE 3. Effect of convective acceleration. (*a*) Acceleration of the free stream: ——, $\partial\tilde{\mathbf{U}}/\partial\tilde{t}$; ------, s. (*b*) The evolution of the drag coefficient with time after subtracting the effect of temporal acceleration as shown in figure 2(*b*), i.e. $\Delta C_{PD} = C_{PD}(\partial\mathbf{U}/\partial t, \nabla\mathbf{U}) - C_{PD}\ (\partial\mathbf{U}/\partial t)$ ——, ΔC_{PD}; ------, ΔC_{VD}.

when compared to (3.2). Figure 3(*b*) shows the time history of the increase in the pressure (ΔC_{PD}) and viscous drag (ΔC_{VD}) coefficients due to the imposed strain, over and above the effect of temporal acceleration of the uniform flow (3.2). In other words, the result shown in figure 2(*b*) has been subtracted and only the difference is plotted in figure 3(*b*) to highlight the effect of strain. Both the uniform and strain-rate components are increased linearly, and correspondingly the pressure drag increases quadratically. The increase in the pressure drag coefficient at $\tilde{t} = 0.025$ is approximately 0.4 and therefore is well-predicted by the inviscid flow result $\frac{4}{3}(1+C_M)s_0$ with $C_M = 1/2$. Other variations of $s(t)$, such as quadratic and exponential, have also been attempted. These changes influence the rate of increase in the drag coefficient over $0 \leqslant \tilde{t} \leqslant 0.025$, but the overall increase in drag depends only on s_0. This is in agreement with Auton *et al.*'s (1988) analysis that in an inviscid flow the force on the sphere is not influenced by the rate of change of of the strain rate.

A number of simulations with simultaneous temporal and convective accelerations of the ambient flow have been performed at different Reynolds numbers and strain magnitudes, and for both axisymmetric and planar strain, which are reported in table 1. In all cases, the inviscid theory with $C_M = 1/2$ is observed to be quite accurate. Also shown in table 1 are the results for planar straining flows with elongational direction oriented at an angle to the X-axis ($\Theta \neq 0$, $\Phi \neq 0$). In these cases, the effect

Strain	Re	s	Computed ΔC_{PD}	ΔC_{PD} from inviscid theory
Axisymmetric	10	0.1	0.192	0.200
Axisymmetric	10	0.2	0.387	0.400
Axisymmetric	50	0.1	0.197	0.200
Axisymmetric	200	0.1	0.207	0.200
Planar, $\Theta = 0$, $\Phi = 0$	10	0.1	0.202	0.200
Planar, $\Theta = 0$, $\Phi = 0$	10	0.2	0.433	0.400
Planar, $\Theta = 0$, $\Phi = 0$	50	0.1	0.207	0.200
Planar, $\Theta = 0$, $\Phi = 0$	100	0.1	0.215	0.200
Planar, $\Theta = 0$, $\Phi = 0$	200	0.1	0.220	0.200
			Computed ΔC_{PL}	ΔC_{PL} from inviscid theory
Planar, $\Theta = \pi/4$, $\Phi = 0$	10	0.1	0.196	0.200
Planar, $\Theta = \pi/4$, $\Phi = 0$	10	0.2	0.392	0.400
Planar, $\Theta = \pi/4$, $\Phi = 0$	50	0.1	0.202	0.200
Planar, $\Theta = \pi/4$, $\Phi = 0$	200	0.1	0.211	0.200
Planar, $\Theta = 0$, $\Phi = \pi/4$	10	0.1	0.103	0.100
Planar, $\Theta = 0$, $\Phi = \pi/4$	50	0.1	0.098	0.100

TABLE 1. Effect of rapid convective acceleration of the ambient flow. The rapid changes in the pressure drag (ΔC_{PD}) and lift (ΔC_{PL}) coefficients over 0 to $\tilde{t}_0$ are listed based on the simulation results and the predictions by the inviscid flow result of Auton *et al.* (1988).

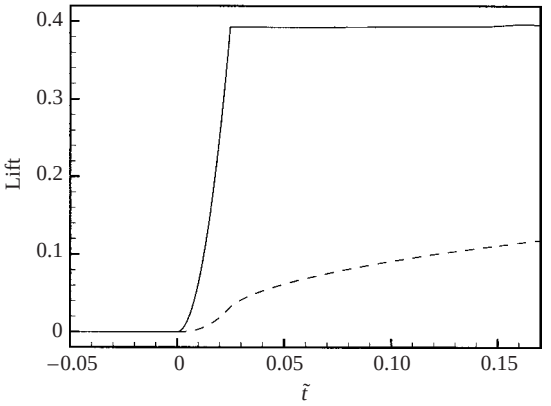

FIGURE 4. Effect of rapid convective acceleration on lift forces. A planar straining flow is imposed at $\Theta = \pi/4$, $\Phi = 0$ orientation and the response of the lift coefficients are shown. ——, C_{PL}; - - - -, C_{VL}.

of strain is to introduce a lift force (Bagchi & Balachandar 2002*a*). The magnitude of the lift force at $\tilde{t}_0$ is consistent with the inviscid flow prediction. For example, the case of $Re = 10$, $s_0 = 0.2$ and $\Theta = \pi/4$, $\Phi = 0$ is shown in figure 4. A rapid increase in the pressure lift coefficient (ΔC_{PL}) of magnitude 0.39 is consistent with the inviscid flow result of $\frac{4}{3}(1 + C_M)s_0$ with $C_M = 1/2$.

3.3. *Effect of viscous saturation*

The above results suggest that the added-mass effects of both temporal and convective accelerations of the ambient flow are similar in nature. However, the similarity is limited to the case of rapid acceleration from an initially stagnant flow. Differences

begin to emerge when the flow is accelerated from a fully developed non-stagnant initial condition. The effect of temporal acceleration is dependent only on the sign and magnitude of acceleration, and is independent of whether the flow is accelerated from a stagnant or a fully developed initial flow. In fact, in the simulations of Chang & Maxey (1995), the initial state was taken as a steady, moderate-Re, fully developed flow. The ambient flow was accelerated from an initial velocity $\tilde{U}_b$ according to

$$\left.\begin{aligned} \tilde{\boldsymbol{U}}(\tilde{t}) &= \tilde{U}_b \boldsymbol{e}_X, \quad \tilde{t} \leqslant 0, \\ \tilde{\boldsymbol{U}}(\tilde{t}) &= \left(\tilde{U}_b + \frac{\tilde{t}}{\tilde{t}_0}\right) \boldsymbol{e}_X, \quad 0 \leqslant \tilde{t} \leqslant \tilde{t}_0, \\ \tilde{\boldsymbol{U}}(\tilde{t}) &= (\tilde{U}_b + 1)\boldsymbol{e}_X, \quad \tilde{t} \geqslant \tilde{t}_0. \end{aligned}\right\} \tag{3.6}$$

The final velocity in dimensionless form is $\tilde{U}_b + 1$. They observed that the sudden change in the pressure drag force at the start or end of the acceleration process was still given by $\frac{4}{3}(1 + C_M)\partial\tilde{\boldsymbol{U}}/\partial\tilde{t}$. Thus, using a fully developed flow as the initial state did not seem to modify the effect of temporal acceleration.

An analogous fully developed initial condition can be considered for the case of convective acceleration as well. Consider the general case of an initial state, where for $\tilde{t} \leqslant 0$ the sphere is held stationary in a steady linear ambient flow of uniform velocity component $\tilde{U}_b \boldsymbol{e}_X$ and strain-rate component $\tilde{\boldsymbol{S}}_b$. For $0 \leqslant \tilde{t} \leqslant \tilde{t}_0$, the ambient flow is rapidly changed to a new state characterized by a uniform component of $(\tilde{U}_b + 1)\boldsymbol{e}_X$ and a strain-rate component of $\tilde{\boldsymbol{S}}_b + \tilde{\boldsymbol{S}}_0$. Hence

$$\left.\begin{aligned} \tilde{\boldsymbol{U}}(\tilde{t}) &= \tilde{U}_b \boldsymbol{e}_X + \tilde{\boldsymbol{X}} \cdot \tilde{\boldsymbol{S}}_b, \quad \tilde{t} \leqslant 0, \\ \tilde{\boldsymbol{U}}(\tilde{t}) &= \left(\tilde{U}_b + \frac{\tilde{t}}{\tilde{t}_0}\right) \boldsymbol{e}_X + \tilde{\boldsymbol{X}} \cdot \tilde{\boldsymbol{S}}(\tilde{t}), \quad 0 \leqslant \tilde{t} \leqslant \tilde{t}_0, \\ \tilde{\boldsymbol{U}}(\tilde{t}) &= (\tilde{U}_b + 1)\boldsymbol{e}_X + \tilde{\boldsymbol{X}} \cdot (\tilde{\boldsymbol{S}}_b + \tilde{\boldsymbol{S}}_0), \quad \tilde{t} \geqslant \tilde{t}_0. \end{aligned}\right\} \tag{3.7}$$

The effect of convective acceleration due to the newly imposed strain $\tilde{\boldsymbol{S}}_0$ can be evaluated by the difference in the changes in computed C_{PD} over $0 \leqslant \tilde{t} \leqslant \tilde{t}_0$ observed with and without $\tilde{\boldsymbol{S}}_0$. In the absence of $\tilde{\boldsymbol{S}}_0$, the inviscid theory (1.2) predicts a change which is given by

$$\Delta C_D(\tilde{\boldsymbol{S}}_0 = 0) = \tfrac{4}{3}(1 + C_M)\left[(\tilde{U}_b + 1)s_b - \tilde{U}_b s_b\right]. \tag{3.8}$$

When $\tilde{\boldsymbol{S}}_0$ is non-zero, (1.2) gives

$$\Delta C_D(\tilde{\boldsymbol{S}}_0 \neq 0) = \tfrac{4}{3}(1 + C_M)\left[(\tilde{U}_b + 1)(s_b + s_0) - \tilde{U}_b s_b\right]. \tag{3.9}$$

Therefore, the effect of the newly imposed strain, according to the inviscid theory, is

$$\Delta C_D(\tilde{\boldsymbol{S}}_0 \neq 0) - \Delta C_D(\tilde{\boldsymbol{S}}_0 = 0) = \tfrac{4}{3}(1 + C_M)s_0(\tilde{U}_b + 1), \tag{3.10}$$

and it arises due to the interaction of $\tilde{\boldsymbol{S}}_0$ with both the initial uniform flow, $\tilde{U}_b \boldsymbol{e}_X$, and the additional uniform flow, $\boldsymbol{e}_X$, resulting from the temporal acceleration. Consider a specific example where $\tilde{U}_b = 1$, the initial $Re = dU_b/\nu = 10$, $\tilde{t}_0 = 0.0025$, $s_b = 0$ and $s_0 = 0.2$. For this case, the rapid increase in the pressure drag coefficient due to the inviscid effect is expected to be twice that seen in figure 3(b). However, over a short time (of the order of $\tilde{t}_0$), the increase is observed to be nearly identical to that shown in figure 3(b). This behaviour is independent of the initial Re, suggesting that the effect of convective acceleration over a short time is only due to the interaction of the rapidly imposed strain, $\tilde{\boldsymbol{S}}_0$, with the rapidly imposed uniform flow, $\boldsymbol{e}_X$. The contribution expected from the interaction of the imposed strain with the fully developed portion

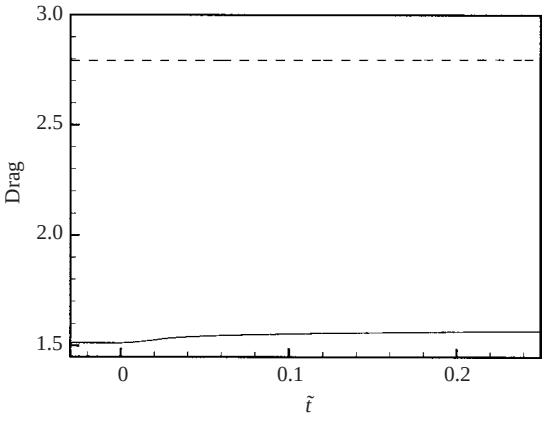

FIGURE 5. Effect of convective acceleration imposed on a viscously developed initial condition. Initial $Re = 10$. ——, C_{PD}; ------, C_{VD}.

of the uniform flow, which was present even before $\tilde{t} = 0$, does not appear on a short time scale.

The above observation is further confirmed with the following test:

$$\left.\begin{aligned} \tilde{\boldsymbol{U}}(\tilde{t}) &= \boldsymbol{e}_X, \quad \tilde{t} \leqslant 0, \\ \tilde{\boldsymbol{U}}(\tilde{t}) &= \boldsymbol{e}_X + \tilde{\boldsymbol{X}} \cdot \tilde{\boldsymbol{S}}(\tilde{t}), \quad 0 \leqslant \tilde{t} \leqslant \tilde{t}_0, \\ \tilde{\boldsymbol{U}}(\tilde{t}) &= \boldsymbol{e}_X + \tilde{\boldsymbol{X}} \cdot \tilde{\boldsymbol{S}}_0, \quad \tilde{t} \geqslant \tilde{t}_0, \end{aligned}\right\} \tag{3.11}$$

where the starting condition is a fully developed, steady and strain-free ambient flow of $\tilde{U}_b = 1$, $Re = 10$. Between $\tilde{t} = 0$ and $\tilde{t}_0 = 0.025$, an axisymmetric straining flow of magnitude $s_0 = 0.2$ is imposed without any temporal acceleration of the uniform component of the ambient flow. Thus, for $\tilde{t} \geqslant \tilde{t}_0$, the ambient flow field is identical to that in figure 3(*a*), and the convective acceleration is the same in both cases. The computed pressure and viscous drag coefficients are shown in figure 5, and can be compared with figure 3(*b*). The difference is striking, since in figure 5 the rapid addition of the strain rate results in almost no increase in drag on a short time scale. Thus, the inertial effect of convective acceleration arising from the interaction of a rapidly imposed strain with a viscously developed uniform flow is somehow nullified by the viscous effects. In the following section, a theoretical analysis is presented to explain the above numerical observations.

3.4. *A theoretical analysis*

Consider the general case of an initially steady linear ambient flow rapidly changed to a new state as defined in (3.7). Let $\tilde{\boldsymbol{u}}_b$ and $\tilde{p}_b$ be the corresponding fully developed initial velocity and pressure fields around the sphere that satisfy the Navier–Stokes equation and the incompressibility condition. The flow $\tilde{\boldsymbol{u}}_b$ approaches the ambient condition as $\tilde{\boldsymbol{x}} \to \infty$ and satisfies the no-slip and no-penetration conditions on the surface of the sphere. For $\tilde{t} \geqslant 0$, let the instantaneous velocity and pressure fields around the sphere be $\tilde{\boldsymbol{u}}$ and $\tilde{p}$. They satisfy the unsteady Navier–Stokes and continuity equations. It is illustrative to write $\tilde{\boldsymbol{u}}$ as

$$\tilde{\boldsymbol{u}} = \tilde{\boldsymbol{u}}_b + \tilde{\boldsymbol{v}}_p + \tilde{\boldsymbol{v}}_v, \tag{3.12}$$

where $\tilde{\boldsymbol{v}}_p$ is the potential flow corresponding to the newly imposed ambient flow, i.e. $\tilde{t}/\tilde{t}_0\,\boldsymbol{e}_X + (\tilde{\boldsymbol{S}}(\tilde{t}) - \tilde{\boldsymbol{S}}_b)\cdot\tilde{\boldsymbol{X}}$. Here $\tilde{\boldsymbol{v}}_p$ satisfies the no-penetration condition

$$\tilde{\boldsymbol{v}}_p \cdot \boldsymbol{n} = 0, \tag{3.13}$$

where $\boldsymbol{n}$ defines the unit normal to the surface of the sphere. The no-slip boundary condition on the surface of the sphere for the newly imposed ambient flow is satisfied by the viscous component $\tilde{\boldsymbol{v}}_v$, and for small $\tilde{t}_0$ the viscous effect is confined to a thin region around the sphere. The Navier–Stokes equation for $\tilde{\boldsymbol{u}}_b$ can be subtracted from that of $\tilde{\boldsymbol{u}}$ to obtain

$$-\nabla\tilde{p} + \nabla\tilde{p}_b \approx \frac{\partial\tilde{\boldsymbol{v}}_p}{\partial\tilde{t}} + \tilde{\boldsymbol{u}}_b\cdot\nabla\tilde{\boldsymbol{v}}_p + \tilde{\boldsymbol{v}}_p\cdot\nabla\tilde{\boldsymbol{v}}_p + \tilde{\boldsymbol{v}}_p\cdot\nabla\tilde{\boldsymbol{u}}_b. \tag{3.14}$$

In the above, contributions from the viscous component $\tilde{\boldsymbol{v}}_v$ are ignored, which for very short times can be justified following the scaling argument given by Mougin & Magnaudet (2001).

Time variations in both the uniform and strain-rate components of the ambient flow are included in $\partial\tilde{\boldsymbol{v}}_p/\partial\tilde{t}$. However, it is only the temporal acceleration of the uniform component that contributes to the drag force. From symmetry arguments it can be shown that the time variation in the strain rate $\tilde{\boldsymbol{S}}$ makes no net contribution. Furthermore, it can be observed that the pressure distribution is linearly dependent on the temporal acceleration, while the convective acceleration's influence is through the nonlinear terms. The last term on the right-hand side of (3.14) accounts for the interaction of the strain-rate component of the initial flow with the potential flow field generated by the newly imposed flow. The second and third terms, respectively, account for the interaction of the newly imposed strain with the initial, viscously developed flow ($\tilde{\boldsymbol{u}}_b$) and the potential field due to the newly imposed flow ($\tilde{\boldsymbol{v}}_p$).

The change in the pressure drag coefficient as the flow is rapidly accelerated from $\tilde{t} = 0$ to $\tilde{t}_0$ can be obtained by integrating (3.14). A few simplifications to this equation are possible. First, the temporal acceleration of the ambient flow is stopped at $\tilde{t}_0$, which implies that

$$\frac{\partial\tilde{\boldsymbol{v}}_p}{\partial\tilde{t}} = 0 \quad \text{for} \quad \tilde{t} > \tilde{t}_0. \tag{3.15}$$

Thus, for $\tilde{t}$ just above $\tilde{t}_0$, only the effect of convective acceleration remains. Second, in order to obtain the pressure drag coefficient, it is sufficient to consider the pressure variation along the surface of the sphere. This will further simplify the evaluation of the nonlinear terms in (3.14).

Consider first a case when the initial flow $\tilde{\boldsymbol{u}}_b$ is a potential flow. On the surface of the sphere, $\tilde{\boldsymbol{u}}_b$ satisfies only the no-penetration condition. Then all three nonlinear terms on the right-hand side of (3.14) are non-zero and contribute to the pressure drag force. Integrating this equation twice over the surface of the sphere, one obtains

$$\Delta C_{PD} = 2(s_b + s_0)(\tilde{U}_b + 1) - 2s_b\tilde{U}_b. \tag{3.16}$$

This is consistent with the inviscid flow result (3.9) using $C_M = 1/2$.

Consider now a case when the initial flow $\tilde{\boldsymbol{u}}_b$ is fully developed. Then, on the surface of the sphere,

$$\tilde{\boldsymbol{u}}_b = 0 \quad \text{and} \quad \nabla\tilde{\boldsymbol{u}}_b = \begin{bmatrix} \partial\tilde{u}_{br}/\partial r & \partial\tilde{u}_{b\theta}/\partial r & \partial\tilde{u}_{b\phi}/\partial r \\ 0 & 0 & 0 \\ 0 & 0 & 0 \end{bmatrix}, \tag{3.17}$$

in spherical coordinates. The potential part of the newly imposed flow satisfies the no-penetration condition, which implies

$$\tilde{\boldsymbol{v}}_p = [0 \quad \tilde{v}_{p\theta} \quad \tilde{v}_{p\phi}]. \tag{3.18}$$

Together, (3.17) and (3.18) imply that on the surface of the sphere

$$\tilde{\boldsymbol{u}}_b \cdot \nabla \tilde{\boldsymbol{v}}_p = 0 \quad \text{and} \quad \tilde{\boldsymbol{v}}_p \cdot \nabla \tilde{\boldsymbol{u}}_b = 0. \tag{3.19}$$

Therefore, the second and the last terms on the right-hand side of (3.14) do not contribute to pressure drag. The only contribution is from the third term. Thus, integrating (3.14) twice, one obtains

$$\Delta C_{PD} = 2s_0. \tag{3.20}$$

Thus, only the interaction between the viscously unsaturated uniform component and the strain-rate component of the new ambient flow (i.e. $\boldsymbol{e}_X \cdot \tilde{\boldsymbol{S}}_0$) is felt immediately over a short time. The added-mass and pressure gradient forces due to $\boldsymbol{e}_X \cdot \tilde{\boldsymbol{S}}_b$ and $\tilde{U}_b \boldsymbol{e}_X \cdot \tilde{\boldsymbol{S}}_0$ are masked by the viscous effects. For $\tilde{t} \gg \tilde{t}_0$, the newly imposed ambient flow also becomes viscously developed. After such a long period there is no difference between the effect of $\boldsymbol{e}_X \cdot \tilde{\boldsymbol{S}}_0$ and other contributions to the convective acceleration. The simulation results presented in figures 2 to 5 and in §§ 3.1 to 3.3 are consistent with the theoretical argument above. It must be emphasized that the above theoretical development is restricted to a solid sphere only because of the use of the no-slip condition on the surface of the sphere.

3.5. *Basset history force*

In the general case, where the ambient flow is given by (3.7), the asymptotic behaviour of the force, for $\tilde{t} \gg \tilde{t}_0$, is dependent only on the end state characterized by the ambient velocity $\tilde{U}_b + 1$ and the strain rate $\tilde{\boldsymbol{S}}_b + \tilde{\boldsymbol{S}}_0$. The corresponding steady force has contributions only from the steady viscous component ($\boldsymbol{F}_{\mathrm{sv}}$) and the inertial components. For $\tilde{t}$ just above $\tilde{t}_0$, the local state of the ambient flow is still characterized by the end state $\tilde{U}_b + 1$ and $\tilde{\boldsymbol{S}}_b + \tilde{\boldsymbol{S}}_0$. As a result, the steady viscous and the inertial forces at $\tilde{t}$ just above $\tilde{t}_0$ are the same as their values as $\tilde{t} \to \infty$. However, the actual force for $\tilde{t} > \tilde{t}_0$ is time-dependent. The transient behaviour is dependent on both the initial state as well as the manner in which the ambient flow is changed to the end state. Such transient behaviour needs to be accounted for by the history force.

For example, the final state of the ambient flow is the same in both (3.3) and (3.11). Therefore, the steady viscous and the inertial forces in both cases are identical. The different behaviour seen in figures 3(*b*) and 5 for $\tilde{t} > \tilde{t}_0$ is then due to the manner in which the end state is reached. Therefore it is appropriate to account for the difference by the history force. Furthermore, for the ambient flow given by (3.3), the inertial forces due to convective acceleration are immediately realized in the pressure drag. On the other hand, for (3.11), although the inertial effects are the same for $\tilde{t} \geqslant \tilde{t}_0$, they are not immediately realized (see figure 5). This suggests that for a viscously developed initial state, the added-mass and pressure gradient effects are masked by the history force.

The history forces for the above cases are shown in figure 6. It is computed by subtracting the steady viscous and inertial forces from the total force. Consider first the case of (3.1) where only temporal acceleration is imposed. The rapid increase in the history force between $\tilde{t} = 0$ and $\tilde{t}_0 = 0.025$ is a direct result of rapid acceleration of the ambient flow. The rapid increase is followed by a slow decay. It is interesting to note that the magnitude of the peak history force is about 25 and is comparable to

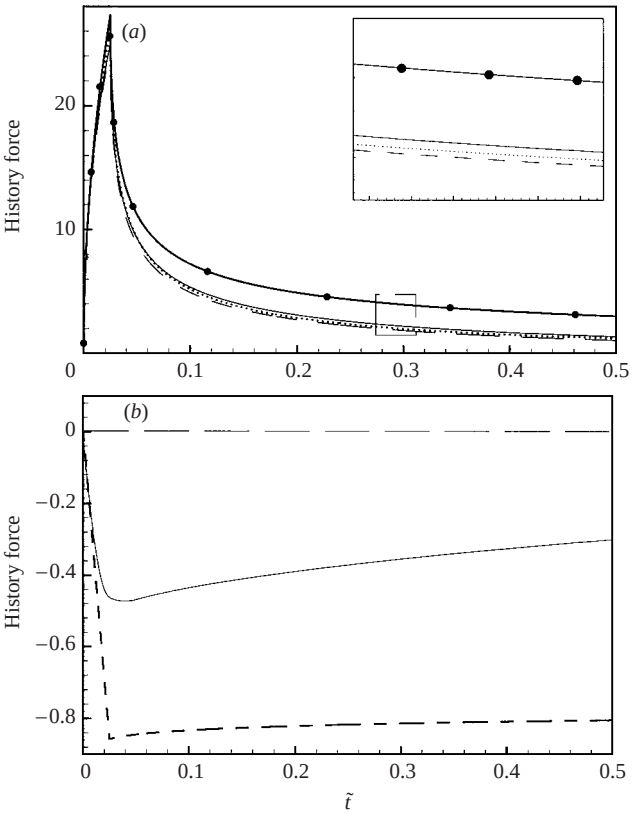

FIGURE 6. The history force in rapidly accelerating flows. (*a*) ——, Computed history force for temporal acceleration from a stagnant initial flow (3.1); - - - - - -, computed history for simultaneous temporal and convective acceleration from a stagnant initial flow (3.3); ·····, prediction by Mei & Adrian's (1992) expression; —●—, prediction by the classical Basset kernel. Note that both the classical kernel and Mei & Adrian's expression cannot differentiate between the cases (3.1) and (3.3). (*b*) ——, History force due to convective acceleration as obtained by the difference between (3.3) and (3.1); - - - - - -, history force due to convective acceleration of a viscously developed flow (3.11); — — —, predictions by the Basset kernel and Mei & Adrian's expression. Note that both these kernels predict a zero history force for the case of (3.11).

the added-mass force. Admittedly, the magnitude of temporal acceleration considered here is large, since our interest is to isolate the inertial forces.

The history force for the case of a rapid change in both the uniform and strain-rate components of the ambient flow, (3.3), corresponding to figure 3(*b*), is also shown in figure 6(*a*). The result differs very little from that of (3.1) as the history force is dominated by the large magnitude of the temporal acceleration, which remains the same in both cases. The history effect of the strain–rate component can be isolated by plotting the difference, which is shown in figure 6(*b*). Between $\tilde{t} = 0$ and $\tilde{t}_0$, it reaches a negative peak and then slowly increases back to zero on a slow time scale. The negative peak corresponds to the difference in the steady viscous component, $\boldsymbol{F}_{\rm sv}$, with and without strain, i.e. $\boldsymbol{F}_{\rm sv} - \boldsymbol{F}^0_{\rm sv}$. In dimensionless terms, the magnitude of the negative peak is equal to 0.48 and corresponds to the difference $C_{D,{\rm sv}}(Re = 10, s_0 = 0.2) - C_{D,{\rm sv}}(Re = 10, s_0 = 0)$. The implication is that the effect of the imposed strain on $\boldsymbol{F}_{\rm sv}$ is viscous in origin and appears only on a slow time scale.

It is of interest to compare the history force obtained from our simulation with the predictions based on the Basset kernel (see (1.3)) and also its moderate-Re extension given by Mei & Adrian (1992) as follows:

$$K(t,\tau) = \left\{ \left[\frac{\pi(t-\tau)\nu}{a^2} \right]^{1/4} + \left[\frac{\pi}{2} \frac{|\boldsymbol{U}_r(\tau)|^3}{a\nu f_H^3(Re_t)} (t-\tau)^2 \right]^{1/2} \right\}^{-2}, \tag{3.21}$$

where $f_H(Re_t) = 0.75 + 0.105Re_t$ and $Re_t = |\boldsymbol{U}_r|d/\nu$. Their predictions for the cases (3.1) and (3.3) are plotted in figure 6(a). For the case of pure temporal acceleration (3.1), the expression given by Mei & Adrian (1992) reproduces the numerical result quite accurately. As expected, the classical Basset kernel predicts a larger history force. However, unlike the numerical results, no difference between the cases (3.1) and (3.3) can be predicted based on these kernels. This is to be expected since the sphere is held fixed, and the only unsteady contribution comes from $\partial U/\partial t$, which is the same for both (3.1) and (3.3).

Finally, the history force for the case of rapidly imposed strain on a fully developed initial state, corresponding to figure 5 and (3.11), is shown in figure 6(b). In this case the history effect is in the absence of any temporal acceleration. It reaches a negative peak at $\tilde{t}_0$ and increases slowly back to zero. Since the inertial forces due to convective acceleration are not realized immediately, the magnitude of the history force is larger than that obtained by the difference between (3.1) and (3.3). The peak value of approximately 0.88 now corresponds to the sum of the difference in the steady viscous components with and without strain, $C_{D,\mathrm{sv}}(Re = 10, s_0 = 0.2) - C_{D,\mathrm{sv}}(Re = 10, s_0 = 0) = 0.48$, and the inertial forces $\frac{4}{3}(1 + C_M)s_0 = 0.4$. Also shown in the figure are the predictions based on the Basset kernel and its moderate-Re extension (3.21), both of which predict that the history force is zero. Thus, the history kernels developed for unsteady uniform flows are not adequate for convective acceleration.

The form of the history force given in (1.4) and (3.21) does not account for all the effects. In a non-uniform ambient flow these effects can be summarized as: (i) the slow development of the permanent viscous effect of strain that ultimately accounts for the dependence of the steady viscous component, $\boldsymbol{F}_{\mathrm{sv}}$, on the strain rate; and (ii) the slow realization of the pressure gradient and added-mass forces when convective acceleration is imposed on a fully (viscously) developed flow. The history force must then be augmented by additional terms of the form $\int K_1(t,\tau)[\boldsymbol{u} \cdot \partial \boldsymbol{S}/\partial\tau]\,\mathrm{d}\tau$ and $\int K_2(t,\tau)[\partial \boldsymbol{u}/\partial\tau \cdot \boldsymbol{S}]\,\mathrm{d}\tau$. Given the complex nature of the history term even in a uniform ambient flow at moderate Re, it can be appreciated that the actual term and the precise form of the kernels (K_1, K_2, etc.) are likely to be quite complex for non-uniform ambient flows.

The magnitude of the history force presented in figure 6(a) is quite large. This is due to the large temporal acceleration arising from the rapidly imposed ambient flows considered here. It must be emphasized that these tests on rapidly imposed acceleration are considered only in order to isolate the inertial forces. Fortunately, in most multiphase flow applications, such high accelerations, and hence large history forces, are unlikely to occur. As will be shown later, the history force is indeed quite small for a freely accelerating sphere in an otherwise steady straining flow.

4. Steady-state results

In the case of a stationary sphere subjected to a steady ambient flow, the only contribution to the inertial force is from convective acceleration. The transient component

of the viscous force (the history) is zero. Equation (1.4) simplifies to

$$\boldsymbol{F} = \boldsymbol{F}_{\rm sv} + m_{\rm f}\,(1 + C_M)\,\boldsymbol{U}\cdot\boldsymbol{S}, \tag{4.1}$$

where $\boldsymbol{U}$ is measured at the centre of the sphere. Knowing the inertial contribution to the overall force, the steady viscous contribution, $\boldsymbol{F}_{\rm sv}$, can be isolated from the steady-state results. In a uniform flow devoid of any spatial gradient ($\boldsymbol{S} = 0$), $\boldsymbol{F}_{\rm sv}$ reduces to the standard drag force (1.5), which is parameterized by the relative velocity only. The computational results of Magnaudet *et al.* (1995) for a stationary sphere subjected to a steady axisymmetric straining flow show that $\boldsymbol{F}_{\rm sv}$ must depend on both the relative velocity and strain rate. For an ambient flow with arbitrary uniform and strain-rate components, $\boldsymbol{F}_{\rm sv}$ can be expected to be influenced by the additional parameters, such as the axisymmetric or planar nature of strain (f_s), and the relative orientation (Θ and Φ) of the strain-rate tensor with respect to the relative velocity vector. In this section we will use all available results on steady straining flow past a stationary sphere to explore the dependence of $\boldsymbol{F}_{\rm sv}$. Specifically, the numerical results of Magnaudet *et al.* (1995) for axisymmetric straining flows and those of Bagchi & Balachandar (2002*a*) for planar straining flows are considered. A wide range of Reynolds numbers and strain-rate magnitudes is examined. Additionally, for the case of planar strain, results at different orientations, Θ and Φ, are also considered.

Using the non-dimensionalization given by (2.9), (4.1) can be written in terms of the drag and lift coefficients. For a general orientation of ambient strain, the drag and lift coefficients are

$$\left.\begin{aligned} C_D &= C_{D,\,\rm sv} + \tfrac{4}{3}(1 + C_M)\,s[(\cos^2\Theta - f_s\sin^2\Theta)\cos^2\Phi + (f_s - 1)\sin^2\Phi],\\ C_{LY} &= C_{LY,\,\rm sv} + \tfrac{4}{3}(1 + C_M)\,\frac{s}{2}\,(f_s + 1)\sin 2\Theta\cos\Phi,\\ C_{LZ} &= C_{LZ,\,\rm sv} + \tfrac{4}{3}(1 + C_M)\,\frac{s}{2}\,[f_s\sin^2\Theta - \cos^2\Theta + (f_s - 1)]\sin 2\Phi, \end{aligned}\right\} \tag{4.2}$$

where the drag coefficient, C_D, is the component in the direction of the relative velocity $\boldsymbol{U}_r$. Since the sphere is stationary, $\boldsymbol{U}_r$ may be assumed to be aligned with the X-direction, without loss of generality. C_{LY} and C_{LZ} are the lift or side force coefficients in the Y- and Z-directions. When the elongational direction of strain is aligned with the direction of $\boldsymbol{U}_r$, i.e. $\Theta = 0$, $\Phi = 0$, only drag is generated and the lift forces are zero. For other orientations of the strain-rate tensor, the lift coefficients may be non-zero. In particular, we consider the cases $\Theta = \pi/4$, $\Phi = 0$ and $\Theta = 0$, $\Phi = \pi/4$. In the former case, C_{LY} is non-zero, while in the latter, C_{LZ} is non-zero.

The computed drag and lift forces from the simulations of Magnaudet *et al.* (1995) and Bagchi & Balachandar (2002*a*) are used in (4.2) to extract the steady viscous contribution: $C_{D,\,\rm sv}$, $C_{LY,\rm sv}$ and $C_{LZ,\,\rm sv}$. These results can be compared with their counterparts in uniform flow: $C^0_{D,\,\rm sv}$, $C^0_{LY,\,\rm sv}$ and $C^0_{LZ,\,\rm sv}$. The standard drag coefficient, $C^0_{D,\,\rm sv}$, is a function of Re alone and is readily obtained from (1.5). For $Re < 210$, the lift coefficients $C^0_{LY,\,\rm sv}$ and $C^0_{LZ,\,\rm sv}$ are known to be zero. At higher Reynolds numbers the sphere wake is non-axisymmetric resulting in a net lift force (Bagchi, Ha & Balachandar 2001). However, the direction of the lift force is arbitrary. Such complications are not central to our discussion, and we shall simply take $C^0_{LY,\,\rm sv} = C^0_{LZ,\,\rm sv} = 0$. The comparison is presented in table 2, where for the aligned cases ($\Theta = 0, \Phi = 0$) only $C_{D,\,\rm sv}$ and $C^0_{D,\,\rm sv}$ are shown. For the non-aligned cases ($\Theta \neq 0$ or $\Phi \neq 0$) both the drag and lift coefficients are compared. Even at a moderate strain-rate magnitude of 0.1, the difference is significant. For the same strain magnitude, the difference is somewhat higher for the planar strain than for

Strain	Re	s	$C^0_{D,\mathrm{sv}}$	$C_{D,\mathrm{sv}}$
Axisymmetric	10	0.1	4.31	4.55
	100	0.1	1.09	1.19
	200	0.1	0.77	0.86
	300	0.1	0.65	0.72
	10	0.2	4.31	4.78
	100	0.2	1.09	1.26
	200	0.2	0.77	0.91
	300	0.2	0.65	0.79
Planar	10	0.1	4.31	4.68
$\Theta = 0, \Phi = 0$	50	0.1	1.57	1.74
	100	0.1	1.09	1.23
	200	0.1	0.77	0.90
	300	0.1	0.65	0.76
	10	0.2	4.31	4.97
	50	0.2	1.57	1.90
	100	0.2	1.09	1.33
	200	0.2	0.77	0.96
	300	0.2	0.65	0.83
	50	0.3	1.57	2.02
			$C^0_{LY,\mathrm{sv}}$	$C_{LY,\mathrm{sv}}$
Planar	10	0.1	0	−0.12
$\Theta = \pi/4, \Phi = 0$	50	0.1	0	−0.21
	100	0.1	0	−0.24
	200	0.1	0	−0.27
	300	0.1	0	−0.28
	50	0.2	0	−0.30
	50	0.3	0	−0.33

			$C^0_{D,\mathrm{sv}}$	$C_{D,\mathrm{sv}}$	$C^0_{LY,\mathrm{sv}}$	$C_{LY,\mathrm{sv}}$
Planar	10	0.1	4.31	4.58	0	−0.07
$\Theta = \pi/8, \Phi = 0$	50	0.1	1.57	1.71	0	−0.13
Planar	10	0.1	4.31	4.13	0	−0.12
$\Theta = 3\pi/8, \Phi = 0$	50	0.1	1.57	1.50	0	−0.17
			$C^0_{D,\mathrm{sv}}$	$C_{D,\mathrm{sv}}$	$C^0_{LZ,\mathrm{sv}}$	$C_{LZ,\mathrm{sv}}$
Planar	10	0.1	4.31	3.65	0	1.24
$\Theta = 0, \Phi = \pi/4$	50	0.1	1.57	1.29	0	0.50
	100	0.1	1.09	0.88	0	0.39
	200	0.1	0.77	0.63	0	0.34
	300	0.1	0.65	0.53	0	0.32
	50	0.2	1.57	1.57	0	0.56
	50	0.3	1.57	1.68	0	0.67

TABLE 2. Comparison of the steady viscous force with and without strain.

axisymmetric strain. The influence of strain rate on $C_{LY,\mathrm{sv}}$ and $C_{LZ,\mathrm{sv}}$ is significant. It was shown in Bagchi & Balachandar (2002*a*) that the direction of the lift force may be opposite to that predicted by the inviscid theory. Accordingly, for the case of $\Theta = \pi/4$, $\Phi = 0$, the steady viscous component of the lift coefficient is observed to be negative.

Based on the simulation results for the aligned axisymmetric straining flows, Magnaudet *et al.* (1995) suggested that the non-inertial effect of strain is primarily on the viscous drag. In other words, if $C_{D,\mathrm{sv}}$ is decomposed into contributions from pressure and viscous shear stress as $C_{PD,\mathrm{sv}}$ and $C_{VD,\mathrm{sv}}$, then Magnaudet *et al.*'s (1995) results suggest that $C_{PD,\mathrm{sv}}$ is not significantly affected by strain, and it depends only on Re. $C_{VD,\mathrm{sv}}$, however, is affected by strain and it needs to be parameterized both in terms of Re and s. The implication is that the strain-induced correction to the pressure drag is primarily inertial in nature, and therefore the effect of strain is accounted for in the added-mass and pressure gradient forces, resulting in $C_{PD,\mathrm{sv}}$ being independent of strain. This observation can be verified for the planar strain as well for varying Re and strain orientation. Similar to (4.2), the pressure drag and lift coefficients can be written as

$$\left.\begin{aligned} C_{PD} &= C_{PD,\mathrm{sv}} + \tfrac{4}{3}(1+C_M)\,s[(\cos^2\Theta - f_s\sin^2\Theta)\cos^2\Phi + (f_s-1)\sin^2\Phi], \\ C_{PLY} &= C_{PLY,\mathrm{sv}} + \tfrac{4}{3}(1+C_M)\frac{s}{2}(f_s+1)\sin 2\Theta\cos\Phi, \\ C_{PLZ} &= C_{PLZ,\mathrm{sv}} + \tfrac{4}{3}(1+C_M)\frac{s}{2}[f_s\sin^2\Theta - \cos^2\Theta + (f_s-1)]\sin 2\Phi. \end{aligned}\right\} \tag{4.3}$$

The pressure component of the total drag and lift forces can be isolated in the simulations. Then the above equations can be used to estimate the pressure coefficients $C_{PD,\mathrm{sv}}$ etc. These quantities are compared in table 3 with the pressure drag and lift coefficients under the uniform flow condition, i.e. $C^0_{PD,\mathrm{sv}}$, $C^0_{PLY,\mathrm{sv}}$ and $C^0_{PLZ,\mathrm{sv}}$. As pointed out by Magnaudet *et al.* (1995), for the case of axisymmetric strain at $Re \geqslant 100$, $C_{PD,\mathrm{sv}} \approx C^0_{PD,\mathrm{sv}}$. However, for the planar strain cases, even at higher Re, $C_{PD,\mathrm{sv}}$ differs from $C^0_{PD,\mathrm{sv}}$ suggesting a viscous effect of strain on the pressure drag. When the strain-rate tensor is not aligned with relative velocity, the viscous effect of strain on pressure lift can be observed in table 3. Hence the parameterization of the steady viscous pressure drag and lift forces also needs to be in terms of both Re and strain. The dependence on strain is not completely unexpected, because at moderate Re, the surface pressure distribution is strongly affected by the presence of strain, and the dependence does not follow the inviscid theory. Further discussion on such effects is given in Bagchi & Balachandar (2002*a*).

The results presented in tables 2 and 3 suggest that $\boldsymbol{F}_{\mathrm{sv}}$ is strongly influenced by the non-uniformity of the ambient flow. The standard drag under uniform flow will not account for the viscous effects of spatial non-uniformity. The representation of $\boldsymbol{F}_{\mathrm{sv}}$ must include the local velocity gradient of the ambient flow. In the following, an invariant representation for $\boldsymbol{F}_{\mathrm{sv}}$ in straining flows is developed followed by an investigation of its behaviour at moderate Re.

5. Parameterization for $\boldsymbol{F}_{\mathrm{sv}}$

The results of the previous section indicate that the steady viscous contribution, $\boldsymbol{F}_{\mathrm{sv}}$, needs to be parameterized both in terms of the relative velocity, $\boldsymbol{U}_r$, and the local velocity gradient, $\nabla\boldsymbol{U}$. From its definition, it can be anticipated that $\boldsymbol{F}_{\mathrm{sv}}$ is independent of unsteadiness in the ambient flow or the sphere (i.e. $\partial\boldsymbol{U}/\partial t$, $\mathrm{d}\boldsymbol{V}/\mathrm{d}t$, $\mathrm{d}\boldsymbol{S}/\mathrm{d}t$, $\mathrm{d}\Omega/\mathrm{d}t$). Such unsteadiness affects the inertial and history forces. $\boldsymbol{F}_{\mathrm{sv}}$ is entirely based on the instantaneous state of the ambient flow characterized by $\boldsymbol{U}_r$ and $\nabla\boldsymbol{U}$. Thus, the starting point of a generalized representation is that $\boldsymbol{F}_{\mathrm{sv}}$ is a vector-valued

Strain	Re	s	$C^0_{PD,\mathrm{sv}}$	$C_{PD,\mathrm{sv}}$
Axisymmetric	10	0.1	1.48	1.55
	100	0.1	0.51	0.51
	200	0.1	0.41	0.41
	300	0.1	0.38	0.38
	10	0.2	1.48	1.60
	100	0.2	0.51	0.50
	200	0.2	0.41	0.41
	300	0.2	0.38	0.39
Planar	10	0.1	1.48	1.62
$\Theta = 0, \Phi = 0$	50	0.1	0.66	0.70
	100	0.1	0.51	0.55
	200	0.1	0.41	0.45
	300	0.1	0.38	0.41
	10	0.2	1.48	1.69
	50	0.2	0.66	0.74
	100	0.2	0.51	0.57
	200	0.2	0.41	0.46
	300	0.2	0.38	0.43
	50	0.3	0.66	0.77
			$C^0_{PLY,\mathrm{sv}}$	$C_{PLY,\mathrm{sv}}$
Planar	10	0.1	0	−0.11
$\Theta = \pi/4, \Phi = 0$	50	0.1	0	−0.18
	100	0.1	0	−0.21
	200	0.1	0	−0.24
	300	0.1	0	−0.25
	50	0.2	0	−0.29
	50	0.3	0	−0.37

			$C^0_{PD,\mathrm{sv}}$	$C_{PD,\mathrm{sv}}$	$C^0_{PLY,\mathrm{sv}}$	$C_{PLY,\mathrm{sv}}$
Planar	10	0.1	1.48	1.59	0	−0.07
$\Theta = \pi/8, \Phi = 0$	50	0.1	0.66	0.70	0	−0.11
Planar	10	0.1	1.48	1.49	0	−0.10
$\Theta = 3\pi/8, \Phi = 0$	50	0.1	0.66	0.67	0	−0.14

			$C^0_{PD,\mathrm{sv}}$	$C_{PD,\mathrm{sv}}$	$C^0_{PLZ,\mathrm{sv}}$	$C_{PLZ,\mathrm{sv}}$
Planar	10	0.1	1.48	1.23	0	0.49
$\Theta = 0, \Phi = \pi/4$	50	0.1	0.66	0.50	0	0.26
	100	0.1	0.51	0.37	0	0.23
	200	0.1	0.41	0.30	0	0.23
	300	0.1	0.38	0.27	0	0.23
	50	0.2	0.66	0.61	0	0.33
	50	0.3	0.66	0.63	0	0.42

TABLE 3. Comparison of the pressure component of the steady viscous force with and without strain.

isotropic function of $\boldsymbol{U}_r$ and $\nabla \boldsymbol{U} = \boldsymbol{S} + \Omega$. The analysis considers a sphere that is held stationary, or moving at a constant speed, and here we will restrict attention to only pure straining flows. The general case of rotational ambient flows is discussed in the Appendix. Following the representation theorem outlined by Wang (1970) and

Smith (1971), $\boldsymbol{F}_{\rm sv}$ can be written as

$$\boldsymbol{F}_{\rm sv} = 3\pi d\mu\, g_1\, \boldsymbol{U}_r + m_{\rm f}\, g_2\, \boldsymbol{U}_r \cdot \boldsymbol{S} + \frac{m_{\rm f}\, d}{|\boldsymbol{U}_r|}\, g_3\, \boldsymbol{U}_r \cdot \boldsymbol{S}^2. \tag{5.1}$$

The quantities g_1, g_2, and g_3 are dimensionless, and are functions of the entire set of independent isotropic scalar invariants that can be formed out of $\boldsymbol{U}_r$ and $\boldsymbol{S}$, which can be chosen as Re, s, f_s, Θ and Φ. The first term on the right of (5.1) corresponds to the Stokes-like drag force. The function g_1 can be interpreted as the correction factor to the Stokes drag for moderate-Re flows. The second and third terms account for contributions arising from the straining flow. They are similar in nature to the inertial forces due to convective acceleration in (1.4), except that in (1.4) we have $\boldsymbol{U} \cdot \nabla \boldsymbol{U}$ instead of $\boldsymbol{U}_r \cdot \nabla \boldsymbol{U}$. The difference, although subtle, is important. In (1.4) the inertial forces due to convective acceleration combine with their counterparts due to temporal acceleration to satisfy Galilean invariance. However, as outlined above, $\boldsymbol{F}_{\rm sv}$ is independent of temporal acceleration. Therefore, in order to be invariant under Gallilean transformation, $\boldsymbol{F}_{\rm sv}$ should depend on $\boldsymbol{U}_r$, and not on $\boldsymbol{U}$ and $\boldsymbol{V}$ independently.

The nature of the drag and lift forces observed at moderate Re under planar (Bagchi & Balachandar 2002*a*) and axisymmetric (Magnaudet *et al.* 1995) strain suggests a complex dependence of g_1, g_2 etc. on Re, s, f_s, Θ and Φ. In this section we consider specific cases of axisymmetric and planar straining flows with orientations of $\Theta = 0$, $\Phi = 0$, $\Theta = \pi/4$, $\Phi = 0$, and $\Theta = 0$, $\Phi = \pi/4$. The simulation results for these cases (Bagchi & Balachandar 2002*a* and Magnaudet *et al.* 1995) are used to extract the steady viscous force, $\boldsymbol{F}_{\rm sv}$, from which the expressions for g_1, g_2 and g_3 are obtained.

For the aligned orientation of $\Theta = 0$, $\Phi = 0$, only the drag force exists, and from (5.1) the steady viscous component of the drag coefficient can be written as

$$C_{D,\,\rm sv} = \frac{24}{Re}\, g_1 + \tfrac{4}{3}\, s\, g_2 + \tfrac{4}{3}\, s^2\, g_3. \tag{5.2}$$

Since Θ and Φ are fixed, g_1, g_2 and g_3 are functions of Re, s and f_s only. It was shown in Bagchi & Balachandar (2002*a*) and Magnaudet *et al.* (1995) that the drag force can be written as a combination of a baseline drag that is independent of strain, and a linearly varying contribution due to strain. The baseline drag is simply the Stokes drag with a moderate-Re correction, which is accounted for in the first term on the right-hand side of (5.2). The linear variation of the drag coefficient strain-rate magnitude suggests that g_3 is not important in the limit $\Theta = 0$, $\Phi = 0$. Hence the dependence of g_2 on Re for both the planar and axisymmetric strains can be extracted from the simulation results. The dependence of g_1 and g_2 with Re is plotted in figure 7(*a*) and their approximate expressions are given in table 4.

Next we consider the example of a planar strain whose elongational direction is aligned at 45° to the relative velocity vector (i.e. $\Theta = \pi/4$, $\Phi = 0$). From (5.1) the steady viscous component of the drag and lift coefficients can be written as

$$C_{D,\,\rm sv} = \frac{24}{Re}\, g_1 + \tfrac{4}{3}\, s^2\, g_3, \qquad C_{LY,\,\rm sv} = \tfrac{4}{3}\, s\, g_2. \tag{5.3}$$

If we let g_1 remain unaffected by strain, then the dependence of g_3 on Re and s can be extracted. The result is plotted in figure 7(*b*). The dependence of g_2 is directly obtained from the lift coefficient and is also presented in figure 7(*b*). Approximate expressions that fit the data are given in table 4. It is interesting to note that even though the second term in the expression for $C_{D,\,\rm sv}$ in (5.3) appears to be quadratic in

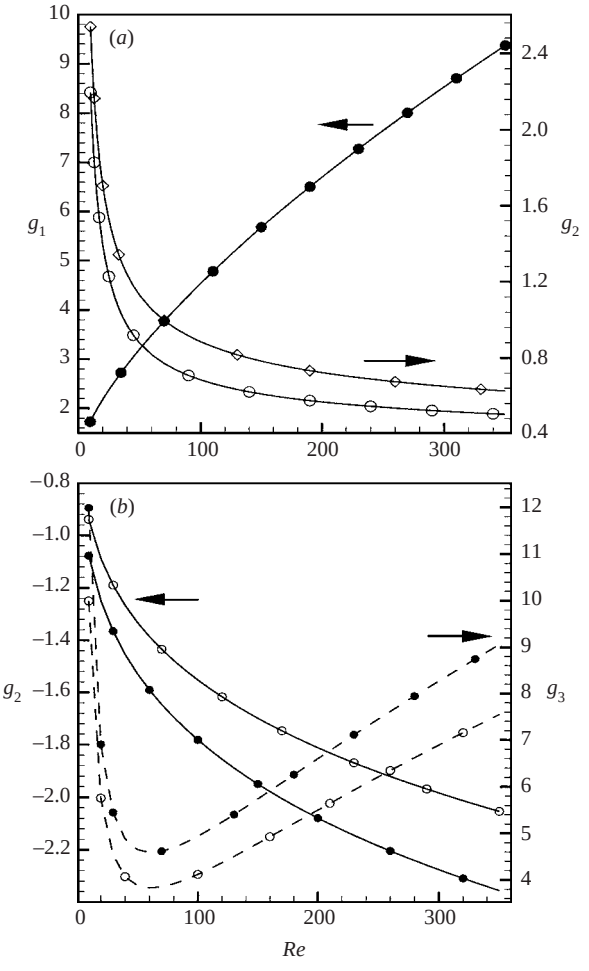

FIGURE 7. The dimensionless functions for the generalized presentation of $\boldsymbol{F}_{\rm sv}$ in straining flows. (*a*) $\Theta = 0, \Phi = 0$: —●—, g_1 (in axisymmetric or planar strain); —○—, g_2 in axisymmetric strain; —◇—, g_2 in planar strain. Note that g_1 and g_2 for this configuration are independent of s. (*b*) $\Theta = \pi/4, \Phi = 0$, planar strain: solid lines indicate g_2; broken lines indicate g_3; data shown here are for two different values of s: ●, $s = 0.1$, and ○, $s = 0.2$.

s, the dependence of g_3 on s as shown in table 4 makes this term linear. Thus, each term of the invariant representation (5.1) corresponds to an independent contribution to the force and must be considered to be on an equal footing.

Next we consider the out-of-plane orientation given by $\Theta = 0$, $\Phi = \pi/4$. The steady viscous component for this orientation takes the following form:

$$C_{D,\rm sv} = \frac{24}{Re} g_1 + \tfrac{2}{3} s g_2 + \tfrac{2}{3} s^2 g_3, \quad C_{LY,\rm sv} = 0, \qquad C_{LZ,\rm sv} = -\tfrac{2}{3}\, s\, g_2 - \tfrac{2}{3}\, s^2\, g_3. \quad (5.4)$$

This case clearly illustrates that g_1 may not always be approximated by the moderate-Re correction to the standard drag in a uniform flow. For this orientation of strain rate we have the constraint

$$C_{D,\rm sv} + C_{LZ,\rm sv} = \frac{24}{Re} g_1. \quad (5.5)$$

Strain	Orientation	$C_{D,\mathrm{sv}}, C_{LY,\mathrm{sv}}$	Functions
Axisymmetric	$\Theta = 0, \Phi = 0$	$C_{D,\mathrm{sv}} = \dfrac{24}{Re} g_1 + \frac{4}{3} s g_2 + \frac{4}{3} s^2 g_3$ $C_{LY,\mathrm{sv}} = C_{LZ,\mathrm{sv}} = 0$	$g_1 = 1 + 0.15 Re^{0.687}$ $g_2 = \dfrac{15}{Re}(1 + 0.06 Re^{0.886})$ $g_3 = 0$
Planar	$\Theta = 0, \Phi = 0$	$C_{D,\mathrm{sv}} = \dfrac{24}{Re} g_1 + \frac{4}{3} s g_2 + \frac{4}{3} s^2 g_3$ $C_{LY,\mathrm{sv}} = C_{LZ,\mathrm{sv}} = 0$	$g_1 = 1 + 0.15 Re^{0.687}$ $g_2 = \dfrac{13.82}{Re}(1 + 0.13 Re^{0.809})$ $g_3 = 0$
Planar	$\Theta = 45^\circ, \Phi = 0$	$C_{D,\mathrm{sv}} = \dfrac{24}{Re} g_1 + \frac{4}{3} s^2 g_3$ $C_{LY,\mathrm{sv}} = \frac{4}{3} s\, g_2,\ C_{LZ,\mathrm{sv}} = 0$	$g_1 = 1 + 0.15 Re^{0.687}$ $g_2 = -\dfrac{1}{Re}(1 + 5.22 Re^{1.223})(1 - 1.0955 s^{0.095})$ $g_3 = \dfrac{11.14}{s\, Re}(1 + 0.002 Re^{1.663})$
Planar	$\Theta = 0, \Phi = 45^\circ$	$C_{D,\mathrm{sv}} = \dfrac{24}{Re} g_1 + \frac{2}{3} s g_2 + \frac{2}{3} s^2 g_3$ $C_{LZ,\mathrm{sv}} = -\frac{2}{3} s\, g_2 - \frac{2}{3} s^2\, g_3$ $C_{LY,\mathrm{sv}} = 0$	$g_1 = (1 + 0.15 Re^{0.687})(1 + 1.7801 s)$ $g_2 + s g_3 = -\dfrac{24}{Re}(1 + 1.41 Re^{0.63})(1 - 0.3 s + 5 s^2)$

TABLE 4. Dimensionless functions used in the parameterization of $\boldsymbol{F}_{\mathrm{sv}}$.

Strain	Re	s	$(24/Re)g_1$	$\frac{4}{3}sg_2$	$\frac{4}{3}s^2g_3$	$\frac{4}{3}(1+C_M)s$
Axisymmetric	10	0.1	4.31 (100%)	0.24 (5.5%)	0	0.2 (4.6%)
	100	0.1	1.09 (100%)	0.10 (9.2%)	0	0.2 (18%)
	200	0.1	0.77 (100%)	0.09 (12%)	0	0.2 (26%)
	300	0.1	0.65 (100%)	0.07 (11%)	0	0.2 (31%)
	10	0.2	4.31 (100%)	0.47 (11%)	0	0.4 (9.3%)
	100	0.2	1.09 (100%)	0.17 (16%)	0	0.4 (37%)
	200	0.2	0.77 (100%)	0.14 (18%)	0	0.4 (52%)
	300	0.2	0.65 (100%)	0.14 (22%)	0	0.4 (62%)
Planar	10	0.1	4.31 (100%)	0.37 (8.6%)	0	0.2 (4.6%)
$\Theta = 0, \Phi = 0$	50	0.1	1.57 (100%)	0.17 (11%)	0	0.2 (13%)
	100	0.1	1.09 (100%)	0.14 (13%)	0	0.2 (18%)
	200	0.1	0.77 (100%)	0.13 (17%)	0	0.2 (26%)
	300	0.1	0.65 (100%)	0.11 (17%)	0	0.2 (31%)
	10	0.2	4.31 (100%)	0.66 (15%)	0	0.4 (9.3%)
	50	0.2	1.57 (100%)	0.33 (21%)	0	0.4 (25%)
	100	0.2	1.09 (100%)	0.24 (22%)	0	0.4 (37%)
	200	0.2	0.77 (100%)	0.19 (25%)	0	0.4 (52%)
	300	0.2	0.65 (100%)	0.18 (28%)	0	0.4 (62%)
	50	0.3	1.57 (100%)	0.45 (29%)	0	0.6 (38%)
Planar	10	0.1	4.31 (100%)	−0.12 (2.8%)	0.16 (3.8%)	0.2 (4.6%)
$\Theta = \pi/4, \Phi = 0$	50	0.1	1.57 (100%)	−0.21 (13%)	0.07 (4.4%)	0.2 (13%)
	100	0.1	1.09 (100%)	−0.24 (22%)	0.08 (7.3%)	0.2 (18%)
	200	0.1	0.77 (100%)	−0.27 (35%)	0.11 (14%)	0.2 (26%)
	300	0.1	0.65 (100%)	−0.28 (43%)	0.14 (22%)	0.2 (31%)
	200	0.2	0.77 (100%)	−0.34 (44%)	0.21 (28%)	0.4 (52%)
	300	0.3	0.65 (100%)	−0.47 (72%)	0.41 (63%)	0.6 (92%)
			$\frac{24}{Re}g_1$		$-\frac{2}{3}sg_2 - \frac{2}{3}s^2g_3$	$\frac{2}{3}(1+C_M)s$
Planar	10	0.1	4.89 (113%)		1.24 (29%)	0.1 (2.3%)
$\Theta = 0, \Phi = \pi/4$	50	0.1	1.79 (114%)		0.50 (32%)	0.1 (6.4%)
	100	0.1	1.27 (117%)		0.39 (36%)	0.1 (9.2%)
	200	0.1	0.97 (126%)		0.34 (44%)	0.1 (13%)
	300	0.1	0.85 (131%)		0.32 (49%)	0.1 (14%)
	50	0.2	2.13 (136%)		0.56 (36%)	0.2 (13%)
	50	0.3	2.35 (150%)		0.67 (43%)	0.3 (19%)

TABLE 5. Absolute and relative magnitude of first- and second-order correction terms due to g_1, g_2 and g_3. The percentage differences compared to Schiller–Neumann drag are given in brackets.

Then g_1 computed based on the above sum of the steady viscous drag and lift forces shows a linear dependence on s, and the best fit to the computational results is shown in table 4. An approximate expression for $g_2 + s\,g_3$ is given in table 4.

The steady viscous drag for a uniform ambient flow, as given in (1.5), is simple and well-established to be accurate over a wide range of Re. In comparison, the expression for the steady viscous drag in a non-uniform ambient flow, as given in (5.1) and table 4, is more complex, due to the added parameters involved, and furthermore is limited to only certain orientations of the strain rate. The relative importance of these added effects of inhomogeneity on the steady viscous force must be established. The magnitudes of the three contributions due to g_1, g_2 and g_3 are shown in table 5. The relative magnitudes of these terms are also expressed as a percentage (shown

within parentheses) of the steady viscous drag of the corresponding uniform flow. Also shown in the table is the inertial force arising from the strain rate. For all cases except when $\Theta = 0, \Phi = \pi/4$, the first term, $(24/Re)g_1$, is the same as the steady viscous drag of the corresponding uniform flow. For the case of $\Theta = 0, \Phi = \pi/4$, the g_1 contribution is higher than the Schiller–Neumann drag by as much as 50%. The percentage contributions from the g_2 and g_3 terms increase with both Re and s. This trend is also the same for the inertial force. In the case of aligned planar strain at low Re, the g_2 contribution is of the same order as the inertial one. As Re increases, the inertial effect begins to dominate. For the non-symmetric case of $\Theta = \pi/4, \Phi = 0$, the effects of g_2 and g_3 are of the order of the inertial effect over the entire range of Re and s considered. Finally, for the case of $\Theta = 0, \Phi = \pi/4$, contributions from g_2 and g_3 are substantially larger than the inertial effect.

6. Unsteady motion of a sphere

Table 4 provides a detailed characterization of the steady viscous component of the drag and lift forces for a straining ambient flow at selected orientations of 0° or 45° to the relative velocity vector. The objective of this section is to evaluate the suitability of such a characterization of the steady viscous force along with the inertial forces in predicting the free translation of a sphere, without accounting for the history force.

Here we will consider simulations of a freely translating sphere in steady axisymmetric or planar straining flows. The sphere is typically released from rest, and it accelerates and attempts to catch up with the ambient flow. The time evolution of the exact drag and lift forces on the sphere is obtained from direct numerical simulations by integrating the surface distribution of the pressure and shear stresses. The exact results are compared with three different estimates based on the instantaneous local flow conditions. The simplest estimate is based on the steady viscous drag for a uniform flow, as given in (1.5), and it ignores all effects of temporal acceleration of the sphere, and the convective acceleration of the ambient flow. This estimate is purely based on the instantaneous relative velocity. In the second estimate we include the inertial forces due to the acceleration of the sphere and the fluid. In the final estimate we also include the viscous effect of straining motion by considering the total force as the sum of the steady viscous drag for non-uniform flow (as given in § 5) and the inertial contribution. The difference between the three estimates will serve to highlight the importance of the effects that have been included progressively. The only effect that has not been included in the third estimate is the history force. As a result, the difference between the third estimate and the exact DNS result will be the history force.

In the direct numerical simulations, the sphere is initially held fixed in a steady linearly varying ambient flow and a fully developed steady solution is obtained. The centre of the sphere is initially located at the origin of the fixed coordinate system ($\boldsymbol{X} = 0$). At $t = 0$, the sphere is released and is allowed to move in response to the hydrodynamic forces acting on it. The motion of the sphere is given by (2.10). The sphere to fluid density ratio (ρ_p/ρ_f) is an important parameter that controls the motion of the sphere. As the sphere moves in the non-uniform flow, the ambient condition at the boundary of the computational domain changes. At each time step, the net flow field is updated using the new boundary condition. The drag and lift forces acting on the sphere are computed at each time step by integrating the pressure and viscous stresses on the surface of the sphere. Three different test cases are chosen:

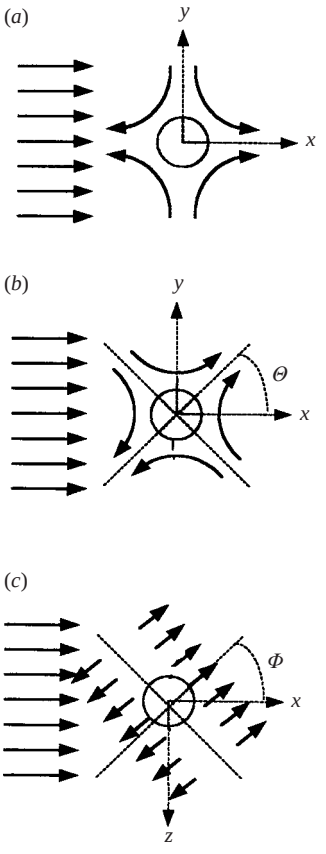

FIGURE 8. Freely moving sphere in linearly varying flows: (*a*) axisymmetric converging flow ($\Theta = 0, \Phi = 0$); (*b*) planar straining flow at $\Theta = \pi/4, \Phi = 0$; (*c*) planar straining flow at $\Theta = 0, \Phi = \pi/4$.

(i) the unidirectional motion of a sphere in an axisymmetric converging stream, (ii) the motion of a sphere in a planar straining flow where the relative velocity lies in the plane of strain, and (iii) the motion of a sphere in a planar straining flow where the relative velocity is at an angle to the plane of strain. The flow configurations for these cases are shown in figure 8.

6.1. *Axisymmetric converging stream*

First we present the results for unsteady unidirectional motion of a freely moving sphere in an axisymmetric straining flow. The ambient flow is given by figure 8(*a*)

$$U_X = U_0 + \sigma X, \quad U_Y = -\frac{\sigma}{2}Y, \quad U_Z = -\frac{\sigma}{2}Z. \tag{6.1}$$

At $t = 0$ the relative velocity of the sphere, $\boldsymbol{U}_r$, and the elongational axis of the strain-rate tensor are aligned with the positive X-axis ($\Theta = 0, \Phi = 0$). Due to the symmetric nature of the flow about the X-axis, the sphere experiences only a drag force along $\boldsymbol{U}_r$, and hence its motion is naturally confined to this axis. First we will consider the case of a sphere to fluid density ratio $\rho_p/\rho_f = 5$. The instantaneous Reynolds number, $Re = |\boldsymbol{U}_r|d/\nu$, and strain magnitude, $s = \sigma d/|\boldsymbol{U}_r|$, are defined based on the

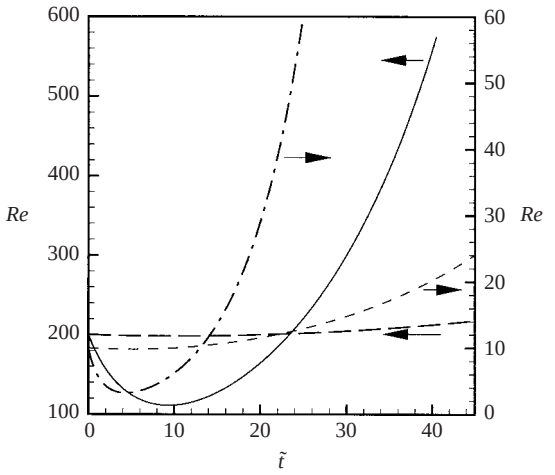

FIGURE 9. The instantaneous sphere Reynolds number in converging flows. On the left scale: ——, initial $Re_0 = 200$, $s_0 = 0.1$, $\rho_p/\rho_f = 5$; — — —, $Re_0 = 200$, $s_0 = 0.1$, $\rho_p/\rho_f = 500$. On the right scale: — - — - —, $Re_0 = 10$, $s_0 = 0.2$, $\rho_p/\rho_f = 5$; - - - -, $Re_0 = 10$, $s_0 = 0.2$, $\rho_p/\rho_f = 500$.

local relative velocity, $\boldsymbol{U}_r = \boldsymbol{U}(\boldsymbol{X}, t) - \boldsymbol{V}(t)$. In the following discussion, a tilde is used when a variable is made dimensionless with respect to the initial relative velocity $\boldsymbol{U}_r(t = 0)$; thus $\tilde{t} = t|\boldsymbol{U}_r(t = 0)|/d$, $\tilde{\boldsymbol{U}} = \boldsymbol{U}/|\boldsymbol{U}_r(t = 0)|$ etc. The initial Reynolds number, based on the initial relative velocity $Re_0 = |\boldsymbol{U}_r(t = 0)|d/\nu$, is 200 and the initial strain magnitude, $s_0 = \sigma d/|\boldsymbol{U}_r(t = 0)|$ is 0.1. The sphere is released at $\tilde{t} = 0$ from a fully developed steady flow field. Under the influence of converging ambient flow, the sphere accelerates continuously. For a short period of time, the relative velocity and hence the instantaneous sphere Reynolds number decreases. However, with time, the fluid velocity increases faster than the sphere velocity and hence the instantaneous Reynolds number increases. Figure 9 shows the instantaneous Re with time. At $\tilde{t} = 40$, the sphere Re reaches 557. Note that at Re greater than about 300, the wake in a uniform flow shows vortex shedding and hence becomes unsteady and three-dimensional. It was shown in Bagchi & Balachandar (2002*b*) that the effect of elongational strain is to stabilize the wake and delay the onset of vortex shedding, and the wake remains axisymmetric. Based on this result, only axisymmetric simulations are performed for the case of converging straining flows considered here.

The temporal behaviour of the unsteady force acting on the sphere is shown in figure 10(*a*). The quantity plotted here is C_D as defined in (2.9) multiplied by $|\tilde{\boldsymbol{U}} - \tilde{\boldsymbol{V}}|^2$, representing the actual force in dimensionless form. The simulation results are compared to the three different estimates of the unsteady force, termed $E1$, $E2$ and $E3$. For the present case of axisymmetric ambient flow, the drag coefficient for the three estimates can be written as

$$E1: \quad C_D^0 = \frac{24}{Re}(1 + 0.15\, Re^{0.687}), \tag{6.2}$$

$$E2: \quad C_D^0 + \tfrac{4}{3}(1 + C_M)\, s\, \frac{|\boldsymbol{U}|}{|\boldsymbol{U} - \boldsymbol{V}|} - \tfrac{4}{3}\, C_M\, \frac{d}{|\boldsymbol{U} - \boldsymbol{V}|^2}\, \frac{\mathrm{d}V}{\mathrm{d}t}, \tag{6.3}$$

$$E3: \quad C_{D,\mathrm{sv}} + \tfrac{4}{3}(1 + C_M)\, s\, \frac{|\boldsymbol{U}|}{|\boldsymbol{U} - \boldsymbol{V}|} - \tfrac{4}{3}\, C_M\, \frac{d}{|\boldsymbol{U} - \boldsymbol{V}|^2}\, \frac{\mathrm{d}V}{\mathrm{d}t}, \tag{6.4}$$

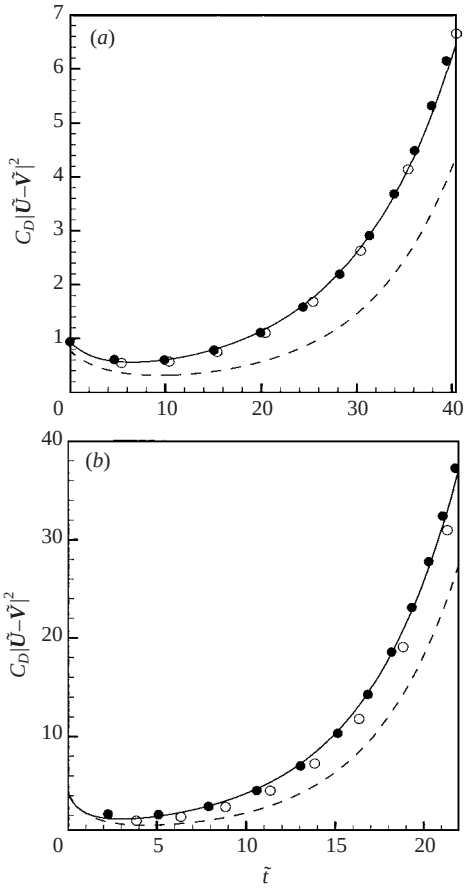

FIGURE 10. Unsteady force on a sphere moving in an axisymmetric converging strain. $\Theta = 0, \Phi = 0$. $\rho_p/\rho_f = 5$. (*a*) Initial $Re_0 = 200, s_0 = 0.1$. (*b*) Initial $Re_0 = 10, s_0 = 0.2$. ——, DNS result; - - - - - -, Schiller–Neumann drag (6.2); ○, prediction by (6.3); and ●, prediction by (6.4).

where C_M is taken to be 1/2 and $C_{D,\mathrm{sv}}$ is given by (5.2) with g_1 and g_2 given in table 4 for the axisymmetric case. As seen in figure 10(*a*), (6.3) and (6.4) capture the time evolution of the unsteady force quite well, indicating that the correction to the steady viscous force due to ambient straining motion is not important for the present case. However, the inclusion of the inertial force is quite important as (6.2) tends to significantly underpredict the force. Furthermore, the good agreement between the DNS result and (6.4) suggests that the history effect is not significant for the present case of a freely moving sphere in a converging flow. This may be due to the fact that in a converging flow the wake activity is significantly suppressed (Magnaudet *et al.* 1995 and Bagchi & Balachandar 2002*a*).

A breakdown of the various contributions to the total force is shown in figure 11(*a*), where the time history of the following forces are plotted: (*a*) the Stokes-like drag given by $(24/Re)\, g_1$; (*b*) the steady viscous contribution from the strain rate given by $(4/3)\, s\, g_2$; (*c*) the inertial force due to local convective acceleration of the fluid given by the second term in (6.4); (*d*) the added-mass force due to the temporal acceleration of the sphere given by the third term in (6.4) and (*e*) the history force.

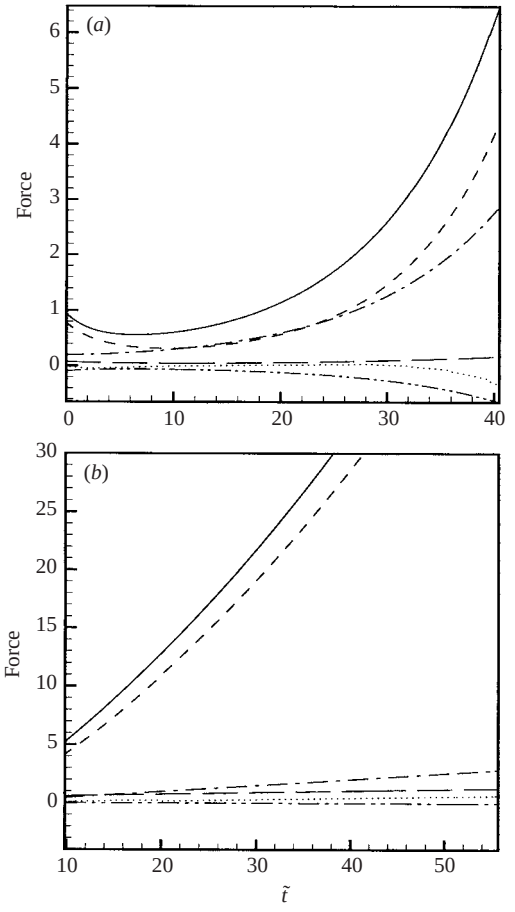

FIGURE 11. Components of the total force in axisymmetric converging flow. (a) Initial $Re_0 = 200$, $s_0 = 0.1$, $\rho_p/\rho_f = 5$. (*b*) Initial $Re_0 = 10$, $s_0 = 0.2$, $\rho_p/\rho_f = 500$. ——, Total force, C_D; - - - - -, contribution from the Stokes-like drag, $24/Re\,g_1$; — — —, contribution of strain to non-inertial force, (4/3), $g_2 s$; – - – - –, inertial forces from convective acceleration, (4/3) $(1 + C_M)s|\boldsymbol{U}|/|\boldsymbol{U} - \boldsymbol{V}|$; – - - – - - –, added-mass force from particle acceleration, (4/3) $C_M(\mathrm{d}\boldsymbol{V}/\mathrm{d}t)\mathrm{d}/|\boldsymbol{U} - \boldsymbol{V}|^2$; $\cdots$, the history force. These quantities are plotted after multiplying by $|\tilde{\boldsymbol{U}} - \tilde{\boldsymbol{V}}|^2$.

The history force is computed as the difference between the DNS result and the estimation from (6.4). It is clear from the figure that the Stokes-like drag and the effect of convective acceleration of the fluid are the two most important quantities. The former can account for nearly 50% of the total force, while the contribution from the latter can be as high as 40%, near the end of the simulation. The contribution arising from the acceleration of the sphere is at the most 9% of the total force. The other contributions, such as that from the history force, are even smaller.

For the present case, the strain-induced viscous correction $(4/3)\,s\,g_2$ is much smaller than the inertial forces. This is not surprising, since in table 5 the g_2 contribution was observed to be about three times less than the inertial forces for a stationary sphere in axisymmetric strain. During the unsteady motion considered here, the g_2 contribution is further reduced. This is due to the fact that this contribution is proportional to the relative velocity $\boldsymbol{U}_r$ (see (5.1)), whereas the inertial effect is proportional to the local

fluid velocity $\boldsymbol{U}$. In an accelerating flow, such as the one considered here, the local fluid velocity is an order of magnitude higher than the relative velocity. Thus, the strain-induced viscous correction is significantly overshadowed by the inertial effect. On the other hand, in cases where the relative velocity and the local fluid velocity are of the same order, such as in the case of a sphere moving close to a stagnation point, the strain-induced viscous correction can be expected to be at least as important as the inertial effect.

A different case with a lower initial sphere Reynolds number of $Re_0 = 10$ and strain magnitude $s_0 = 0.2$ is considered next. The sphere to fluid density ratio is $\rho_p/\rho_f = 5$, which is the same as in the previous example. As before, the sphere is released at $\tilde{t} = 0$ and it accelerates continuously under the converging straining flow. At first, the acceleration of the sphere is high and the relative velocity decreases. The instantaneous Reynolds number decreases to 3.2 at $\tilde{t} = 4.5$ (see figure 9). Beyond this, the relative velocity starts increasing and at $\tilde{t} = 22$, the sphere Reynolds number reaches 37. The unsteady drag measured from the simulation and the predictions by (6.2)–(6.4) are shown in figure 10(*b*). The general trend is similar to the previous case of $Re_0 = 200$ shown in figure 10(*a*). The contribution from the strain-induced viscous correction g_2 is now somewhat increased. This behaviour is consistent with the low-Re result seen in table 5.

The case of a higher density ratio of $\rho_p/\rho_f = 500$ is considered next for an initial Reynolds number of $Re_0 = 200$ and $s_0 = 0.1$. The variation of the instantaneous sphere Reynolds number with time is shown in figure 9. Unlike the low-density cases described above, the heavy sphere accelerates slowly. As a result, the relative velocity increases at a slower rate and at $\tilde{t} = 44$, the sphere Reynolds number is not much higher than 200. The time evolution of the drag force on the sphere is shown in figure 12(*a*). For such a heavy particle the pressure gradient and added-mass forces are often dismissed as being small. However, from figure 12(*a*) it is clear that (6.2) significantly underpredicts the drag force. The inertial forces make a substantial contribution to the total drag force and it arises mostly from the convective acceleration due to the ambient strain rate. The strain-induced viscous correction g_2, although smaller in magnitude than the inertial effect, is not entirely negligible and its inclusion improves the estimation of the total drag force. As in the previous cases the history force remains small and its neglect appears to be well justified. A similar observation can be made in figure 12(*b*) where results for the case of initial $Re_0 = 10$ and $s_0 = 0.2$ are shown for a density ratio 500.

The detailed breakdown of the different components of the net force for the case of $\rho_p/\rho_f = 500$ with initial $Re_0 = 10$ and $s_0 = 0.2$ is shown in figure 11(*b*). As expected, the Stokes-like contribution associated with the function g_1 is the dominant component. All other contributions are significantly less. Nevertheless, of the remaining components, the inertial contribution from the convective acceleration is the largest.

6.2. *Planar straining flow at* $\Phi = 0$

The example considered next is the free translation of a sphere in a planar straining flow at an angle to the principal axes of strain rate. The flow configuration for this case is shown in figure 8(*b*). The ambient flow is given by

$$U_X = U_0 + \sigma Y, \quad U_Y = \sigma X, \quad U_Z = 0. \tag{6.5}$$

The converging direction of the straining flow is oriented at 45° to the positive X-axis. At $\tilde{t} = 0$, the centre of the sphere coincides with $\boldsymbol{X} = 0$: until this time the sphere

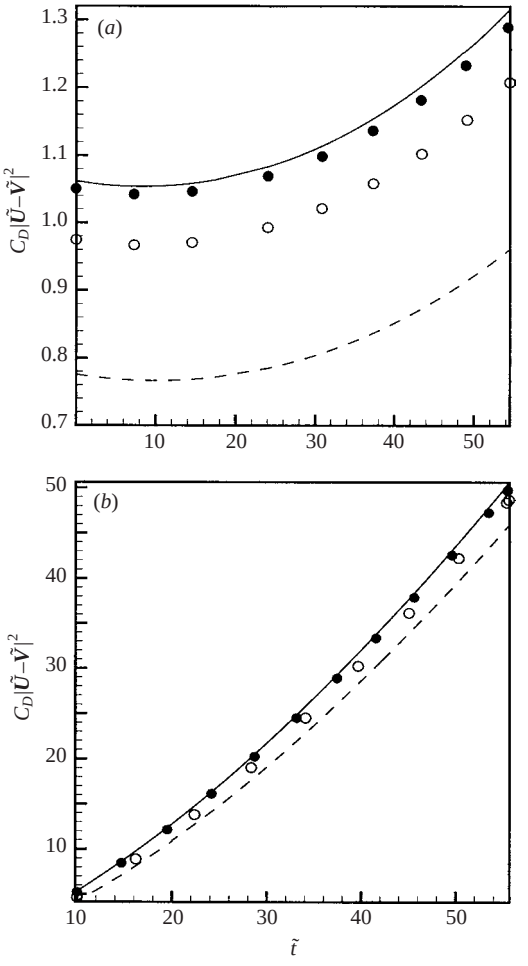

FIGURE 12. Unsteady force on a heavy sphere of $\rho_p/\rho_f = 500$ moving in an axisymmetric strain. (*a*) Initial $Re_0 = 200, s_0 = 0.1$. (*b*) Initial $Re_0 = 10, s_0 = 0.2$. ——, DNS result; - - - - - - -, Schiller–Neumann drag (6.2); ○, prediction by (6.3); ●, prediction by (6.4).

is held fixed. The initial flow field at $\tilde{t} = 0$ is a quasi-steady solution for a constant relative velocity and corresponds to the initial values $Re_0 = 200$ and $s_0 = 0.1$. At $\tilde{t} = 0$ the relative velocity is taken to be aligned with the positive X-axis. Thus, at $\tilde{t} = 0$, the angle between the relative velocity and the converging direction of strain is $\Theta = 45°$. In this configuration, the sphere experiences both the drag and lift forces. As a result, the free motion of the sphere is no longer rectilinear. For $\tilde{t} \geqslant 0$, the sphere is allowed to freely translate in response to the hydrodynamic forces acting on it. As it moves in the straining flow, both the magnitude and direction of the relative velocity change. As a result, the angle Θ between the relative velocity vector and the straining flow changes with time. Figure 13(*a*) shows the sphere trajectory obtained from the direct numerical simulation for the case of $\rho_p/\rho_f = 5$. At the start, the centre of the sphere is located at the origin shown near the bottom left corner of the figure. At $\tilde{t} = 20$, it is located at $X/d \approx 13, Y/d \approx 5$. The instantaneous sphere Reynolds number and the angle Θ are plotted in figure 13(*b*). The variation of Re over time is similar to the

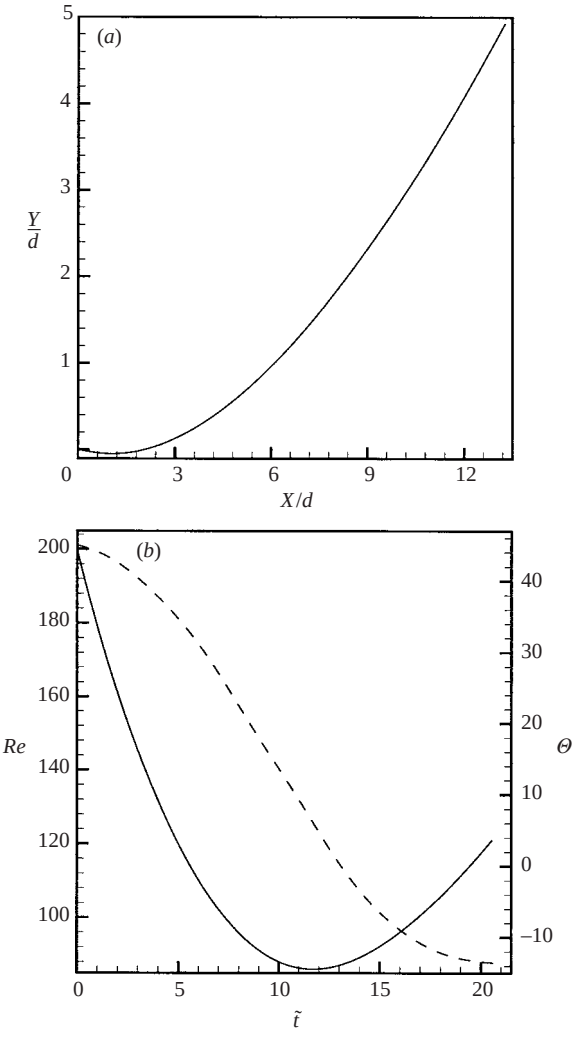

FIGURE 13. Unsteady motion of a sphere in a planar straining flow at initial $\Theta = \pi/4$. Initial $Re_0 = 200$, $s_0 = 0.1$ and $\rho_p/\rho_f = 5$. (*a*) Particle trajectory. (*b*) ——, instantaneous Reynolds number; and - - - - - -, instantaneous relative angle Θ.

previous cases, i.e. an initial decrease in Re followed by a continuous increase. The angle Θ changes from its initial value of 45° to −14° at $\tilde{t} = 20$.

As before, the three different estimates of the drag and lift coefficients for this configuration can be written as

$$E1: \quad C_D^0 = \frac{24}{Re}(1 + 0.15\,Re^{0.687}), \quad C_L = 0, \tag{6.6}$$

$$E2: \quad C_D = C_D^0 + IF_D, \quad C_L = IF_L, \tag{6.7}$$

$$E3: \quad C_D = C_{D,\mathrm{sv}} + IF_D, \quad C_L = C_{L,\mathrm{sv}} + IF_L, \tag{6.8}$$

where the inertial components IF_D and IF_L are given by

$$IF_D = \tfrac{4}{3}(1 + C_M)\, s\, \frac{\boldsymbol{U}_\parallel \cos 2\Theta + \boldsymbol{U}_\perp \sin 2\Theta}{|\boldsymbol{U}_r|} - \tfrac{4}{3} C_M\, \frac{d}{|\boldsymbol{U}_r|^2} \frac{\mathrm{d}\boldsymbol{V}_\parallel}{\mathrm{d}t}, \tag{6.9}$$

$$IF_L = \tfrac{4}{3}(1 + C_M)\, s\, \frac{\boldsymbol{U}_\parallel \sin 2\Theta - \boldsymbol{U}_\perp \cos 2\Theta}{|\boldsymbol{U}_r|} - \tfrac{4}{3} C_M\, \frac{d}{|\boldsymbol{U}_r|^2} \frac{\mathrm{d}V_\perp}{\mathrm{d}t}. \tag{6.10}$$

Here the drag force is in the direction of the instantaneous relative velocity and the lift force is perpendicular to it. The symbols $\parallel$ and $\perp$ are used to indicate the components parallel and perpendicular to $\boldsymbol{U} - \boldsymbol{V}$. The steady viscous components, $C_{D,\mathrm{sv}}$ and $C_{L,\mathrm{sv}}$, are computed using (5.1) and can be written as

$$C_{D,\mathrm{sv}} = \frac{24}{Re}\, g_1 + \tfrac{4}{3}\, g_2\, s\, \cos 2\Theta + \tfrac{4}{3}\, g_3\, s^2, \tag{6.11}$$

$$C_{L,\mathrm{sv}} = \tfrac{4}{3}\, g_2\, s\, \sin 2\Theta. \tag{6.12}$$

Note that the functions g_1, g_2 and g_3 are now dependent on the instantaneous Re, s and Θ. Steady-state simulations, similar to those reported in § 5, over a range of Re and s at $\Theta = 0, \pi/8$ and $\pi/4$ are used to compute these functions. For any intermediate Θ, their values are obtained by interpolation. Also note that the values of these functions at negative Θ can be obtained from those of positive Θ by appropriate symmetry.

The above three estimates along with the exact DNS results are shown in figure 14. Here the X- and Y-components of the total force coefficient are plotted as a function of time after multiplication by $|\tilde{\boldsymbol{U}} - \tilde{\boldsymbol{V}}|^2$. As in the previous examples, the use of (6.6) leads to a significant underprediction of both the X and Y components of the force. Inclusion of the inertial terms as in (6.7) improves the estimation. However, (6.7) still underpredicts the X force between $5 < \tilde{t} < 15$, and significantly overpredicts the Y force at the beginning. The estimate is further improved when the strain-induced viscous correction terms g_2 and g_3 are included, as given by (6.8). The difference between the estimation based on (6.8) and the DNS results suggests that the history force, although not entirely negligible, still remains small. The detailed breakdown of the various contributions to the total force is shown in figure 15. It can be seen that the inertial effect of ambient strain rate is a dominant force comparable to the Schiller–Neumann drag (6.6). In the X-component of the force, the g_2 contribution may be nearly 30%, while the g_3 contribution can be as high as 43%. In the Y-component of the force, the g_2 contribution constitutes nearly the entire viscous force at the beginning. Near the end, the g_2 contribution drops, while the g_3 contribution becomes 35% of the total force. Contributions from the acceleration of the sphere and the history force are much smaller.

6.3. *Planar straining flow at* $\Theta = 0$

Next we consider another example of planar straining flow where the relative velocity is at an angle to the plane of strain (figure 8*c*). The ambient flow is given by

$$U_X = U_0 + \frac{\sigma}{2}(X - Z), \quad U_Y = -\sigma Y, \quad U_Z = \frac{\sigma}{2}(-X + Z). \tag{6.13}$$

The plane of strain makes a 45° angle to the positive X-axis. Until $\tilde{t} = 0$, the sphere is held fixed at $\boldsymbol{X} = 0$. The initial flow field at $\tilde{t} = 0$ is taken as a quasi-steady solution that corresponds to an initial $Re_0 = 300$, $s_0 = 0.1$. In this configuration, the sphere experiences forces along the X- and Z-axes (see §§ 4 and 5). The sphere is released at $\tilde{t} = 0$ and allowed to freely translate under the hydrodynamic force. At $\tilde{t} = 0$, the

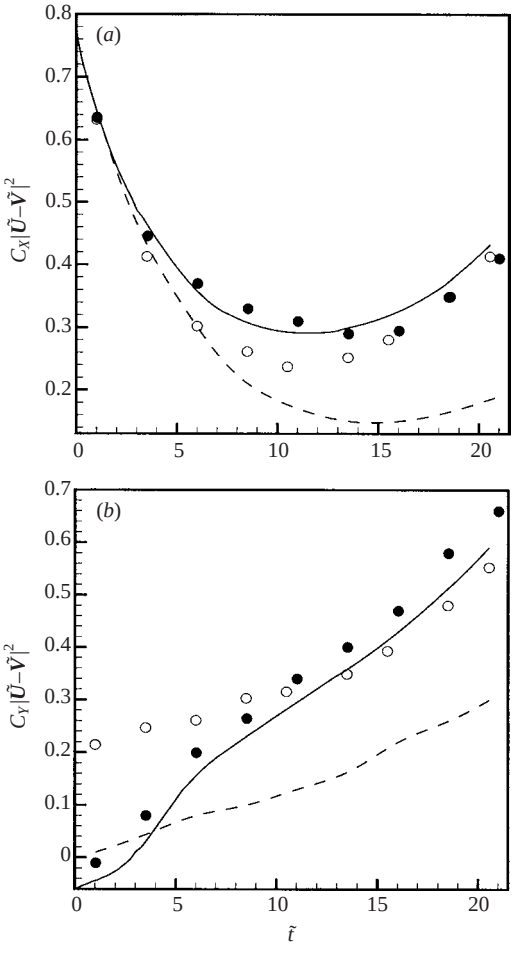

FIGURE 14. Unsteady force on a sphere moving in a planar straining flow. Initial $Re_0 = 200$, $s_0 = 0.1$, and $\rho_p/\rho_f = 5$. (*a*) Force in the X-direction; (*b*) force in the Y-direction. ——, DNS result; - - - - - - - -, prediction by the Schiller–Neumann drag (6.6); ○, prediction by (6.7); ●, prediction by (6.8).

angle between the relative velocity and the plane of strain is $\Phi = 45°$. As the sphere moves in the straining flow, the angle Φ changes with time.

The three estimates of the drag and lift coefficients for this configuration can be written as

$$E1: \quad C_D^0 = \frac{24}{Re}(1 + 0.15\,Re^{0.687}), \quad C_L = 0, \tag{6.14}$$

$$E2: \quad C_D = C_D^0 + IF_D, \quad C_L = IF_L, \tag{6.15}$$

$$E3: \quad C_D = C_{D,\mathrm{sv}} + IF_D, \quad C_L = C_{L,\mathrm{sv}} + IF_L, \tag{6.16}$$

where the inertial components IF_D and IF_L are given by

$$IF_D = \tfrac{2}{3}(1 + C_M)\,s\,\frac{\boldsymbol{U}_\parallel \cos^2\Phi - \boldsymbol{U}_\perp \sin\Phi\cos\Phi}{|\boldsymbol{U}_r|} - \tfrac{4}{3}C_M\,\frac{d}{|\boldsymbol{U}_r|^2}\frac{\mathrm{d}\boldsymbol{V}_\parallel}{\mathrm{d}t}, \tag{6.17}$$

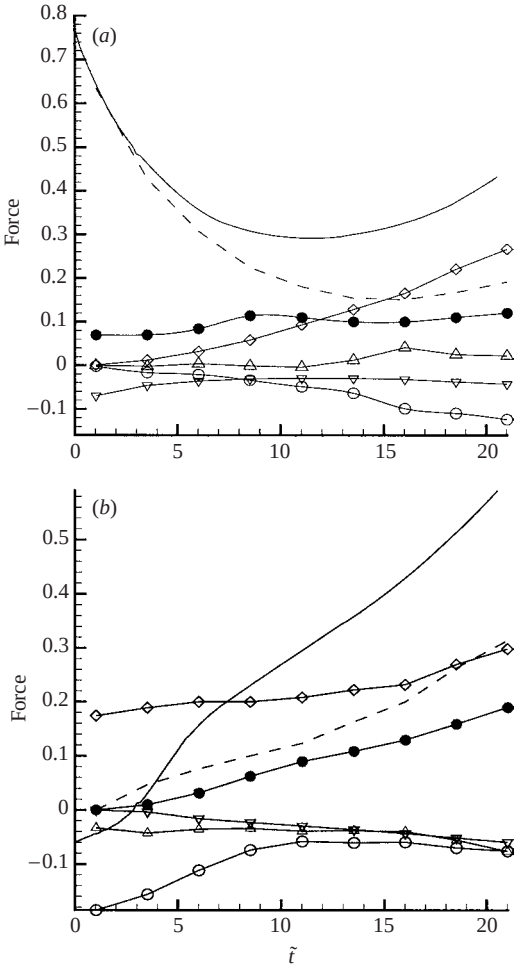

FIGURE 15. Contributions to the total force on the sphere moving in the planar straining flow. $Re_0 = 200$, $s_0 = 0.1$, and $\rho_p/\rho_f = 5$: (*a*) forces in the X-direction; (*b*) forces in the Y-direction. ——, Total force (from DNS result); ------, contribution from g_1 (Schiller–Neumann drag); ●, contribution from g_3; ○, contribution from g_2; ◇, contribution from convective acceleration; ▽, contribution from particles's acceleration; △, transient non-inertial force (history).

$$IF_L = \tfrac{2}{3}(1 + C_M)\, s\, \frac{-\boldsymbol{U}_{\parallel} \sin \Phi \cos \Phi + \boldsymbol{U}_{\perp} \sin^2 \Phi}{|\boldsymbol{U}_r|} - \tfrac{4}{3} C_M \frac{d}{|\boldsymbol{U}_r|^2} \frac{\mathrm{d}V_{\perp}}{\mathrm{d}t}. \tag{6.18}$$

Here the drag force is along the direction of the instantaneous relative velocity and the lift force is perpendicular to it. The symbols $\parallel$ and $\perp$ are again used to indicate the components parallel and perpendicular to $\boldsymbol{U} - \boldsymbol{V}$. The steady viscous components, $C_{D,\mathrm{sv}}$ and $C_{L,\mathrm{sv}}$, are again computed using the expression (5.1) and can be written as

$$C_{D,\mathrm{sv}} = \frac{24}{Re}\, g_1 + \tfrac{4}{3}\, s\, \cos^2 \Phi\, (g_2 + s g_3), \tag{6.19}$$

$$C_{L,\mathrm{sv}} = -\tfrac{4}{3}\, s\, \sin \Phi \cos \Phi\, (g_2 + s g_3). \tag{6.20}$$

Note that the functions g_1, g_2 and g_3 are dependent on the instantaneous values of Re, s and Φ. Steady-state simulations, similar to those reported in § 5, over a range

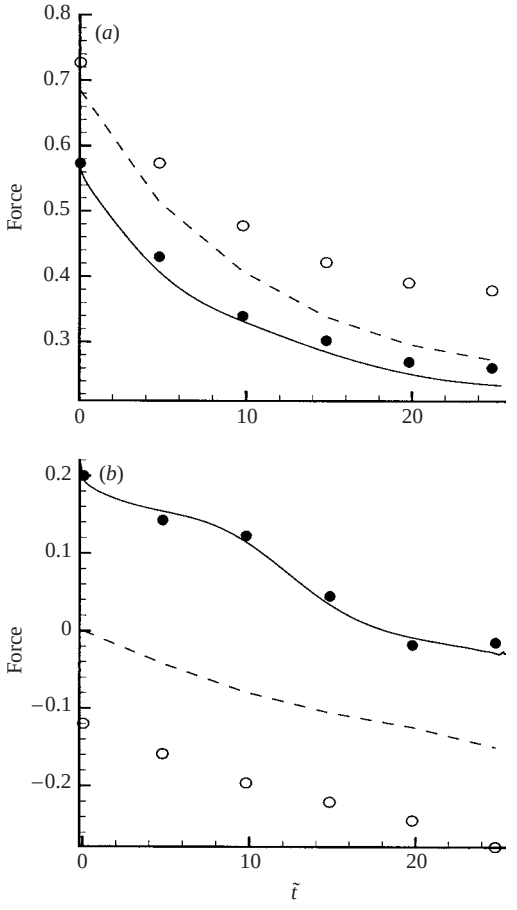

FIGURE 16. Unsteady force on a sphere moving in a $\Phi = \pi/4, \Theta = 0$ planar straining flow. Initial $Re_0 = 300$, $s_0 = 0.1$, and $\rho_p/\rho_f = 5$. (*a*) Force in the X-direction, $C_X(\tilde{U} - \tilde{V})^2$; (*b*) force in the Z-direction, $C_Z(\tilde{U} - \tilde{V})^2$. ——, DNS result; - - - - - -, prediction by the Schiller–Neumann drag (6.14); ○, prediction by (6.15); ●, prediction by (6.16).

of Re and s at different $\Phi = 0, \pi/8$ and $\pi/4$ are used to compute these functions (Bagchi & Balachandar 2002*a*). For any intermediate Φ, their values are obtained by interpolation.

The above three estimates along with the exact DNS results are shown in figure 16. Here the X- and Z-components of the total force coefficient are plotted as a function of time after multiplication by $|\tilde{\boldsymbol{U}} - \tilde{\boldsymbol{V}}|^2$. It is clear from the figure that the use of (6.14) leads to overprediction of the X-component and underprediction of the Z-component of force. Most interestingly, unlike in the previous two examples, the inclusion of the inertial terms worsens the prediction. However, the exact DNS result can be approximated well when the strain-induced corrections given by g_2 and g_3 are retained.

The detailed breakdown of the various contributions to the total force is shown in figure 17. In the X-component, the significant contributions come from g_1, g_2 and g_3. The inertial contributions are much smaller. Also note that the g_1 term can be different from the Schiller–Neumann correction (see § 5). In the Z-component, the

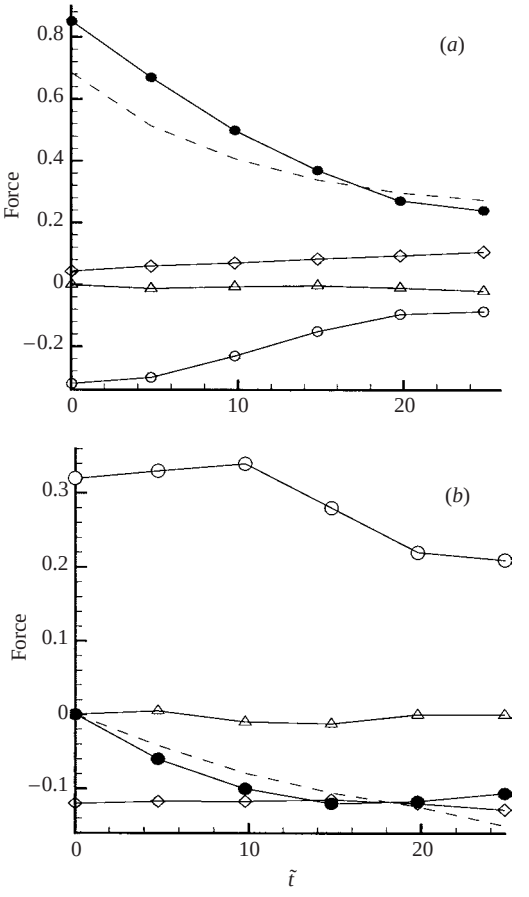

FIGURE 17. Breakdown of various contributions to the total force on the sphere moving in the $\Phi = \pi/4, \Theta = 0$ planar straining flow. $Re_0 = 300, s_0 = 0.1$, and $\rho_p/\rho_f = 5$. (*a*) Forces in the X-direction, and (*b*) forces in the Z-direction. - - - - - - -, Contribution from Schiller–Neumann drag; –●–, contribution from g_1; –○–, contribution from g_2 and g_3; –◇–, contribution from inertial force (added-mass + pressure gradient); –△–, history force.

major contribution comes from the g_2 and g_3 terms. At first, the g_1 contribution is small, and the inertial contribution comprises the rest of the force. Near the end, the g_1 contribution is of the same order as the inertial one. The history force remains negligible in both the X- and Z-components.

7. Conclusion

In this paper we have numerically investigated the effect of spatial non-uniformity in the ambient flow on the equation of motion of a sphere at moderate sphere Reynolds number. A pseudospectral-based DNS methodology is used to solve the detailed flow field around a freely translating sphere in a linearly varying ambient flow ($\nabla \boldsymbol{U}$ = constant). The ambient flow considered here is irrotational and the sphere Re is in the range 10 to 300. Different contributions to the total force on the sphere, namely the inertial (the added-mass and pressure gradient) forces, the steady viscous force, and the unsteady viscous force (history force), are numerically estimated in a

systematic way in the context of ambient straining flows. The objective of the paper is four-fold:

(*a*) To isolate the added-mass force due to convective acceleration of the ambient flow.

(*b*) To establish the effect of ambient strain on the steady viscous force and obtain a parameterization for $\boldsymbol{F}_{sv}$ for a few chosen orientations of the ambient strain rate.

(*c*) To validate the parameterization under unsteady conditions by considering a DNS of a freely translating sphere in straining ambient flows.

(*d*) To estimate the history force in non-uniform irrotational flows.

The important results are summarized below.

(*a*) Added-mass force: In a non-uniform flow, such as the straining flow considered here, the isolation of the added-mass force from the total is difficult since the ambient strain modifies not only the inertial forces, but also the viscous forces. In axisymmetric straining flows, the difference between the pressure drag with and without strain is nearly equal to the added-mass effect, which was exploited by Magnaudet *et al.* (1995) in establishing the added-mass coefficient. However, this is not the case for planar strain, particularly when the strain is oriented at an angle to the relative velocity. Therefore, in order to isolate the added-mass forces under such conditions, we consider DNS of rapidly imposed straining flows past a sphere. By monitoring the rapid changes in the drag and lift forces on the sphere over a short time scale in response to the rapidly imposed external strain, we isolate the inertial effect due to the convective acceleration of the ambient flow.

This methodology is similar to that used by Rivero *et al.* (1991) and Chang & Maxey (1995) where they considered the inertial effect of temporal acceleration in a uniform ambient flow. Here we extended this methodology to consider straining flows. The DNS results show that the added-mass effect at moderate Re arising from convective acceleration of the ambient flow follows the inviscid flow results. A wide variety of straining flows are considered over a range of Re, and for all the cases the inviscid theory is shown to be applicable.

(*b*) Steady viscous force: Knowing the inertial forces we proceed to estimate the effect of ambient strain rate on the steady viscous force. Numerical results for steady axisymmetric (Magnaudet *et al.* 1995) and planar straining flows (Bagchi & Balachandar 2002*a*) past a stationary sphere are used to estimate the steady viscous force $\boldsymbol{F}_{sv}$. Under steady conditions, the history force is zero. Then $\boldsymbol{F}_{sv}$ can be isolated by subtracting the inertial forces from the total drag and lift. In a uniform ambient flow, $\boldsymbol{F}_{sv}$ is represented well by the Schiller–Neumann drag. In the presence of ambient strain, it is shown here that $\boldsymbol{F}_{sv}$ is significantly influenced by and strongly dependent on the magnitude and orientation of the strain rate.

A parameterization for $\boldsymbol{F}_{sv}$ in terms of relative velocity and the local velocity gradient is presented. At low Re, when the principal direction of the strain rate is aligned with the direction of relative velocity, the strain-induced viscous corrections to $\boldsymbol{F}_{sv}$ are comparable to the inertial forces. With increasing Re the inertial forces outweigh the viscous corrections. However, when the principal directions of the strain rate are not aligned with the direction of relative velocity, the strain-induced viscous corrections to $\boldsymbol{F}_{sv}$ can be strong and more important than the inertial forces.

(*c*) DNS of a freely translating sphere: The importance of the inertial forces and the strain-induced modifications to $\boldsymbol{F}_{sv}$ is further validated by considering the unsteady motion of a rigid sphere. Direct numerical simulations of a freely translating sphere in axisymmetric and planar straining flows are performed. The exact unsteady

forces obtained from the DNS are compared with three different estimates: (i) the Schiller–Neumann drag, (ii) the Schiller–Neumann drag, plus the inertial forces, and (iii) the Schiller–Neumann drag, plus the strain-induced correction to $\boldsymbol{F}_{sv}$, plus the inertial forces. Here it must be stressed that while the Schiller–Neumann drag and the inertial forces are well-established, the dependence of $\boldsymbol{F}_{sv}$ on ambient strain is quite complex. The parameterization for $\boldsymbol{F}_{sv}$ obtained here is limited to only axisymmetric and planar strains and is valid only over a limited range of Re, strain-rate magnitudes and orientations. It is thus of interest to examine when the strain-induced correction to $\boldsymbol{F}_{sv}$ is important, for otherwise the estimation can be based on the Schiller–Neumann drag, plus the inertial forces alone.

For all the cases considered, the estimation based on the Schiller–Neumann drag significantly deviates from the exact results. In most cases, the inclusion of the inertial forces significantly improves the estimation of the actual forces. In cases where the motion of the sphere is aligned with the extensional direction of the ambient strain rate, the inertial forces generally outweigh the strain-induced corrections in $\boldsymbol{F}_{sv}$. As a result, a satisfactory prediction of the total force can be made based on only the Schiller–Neumann drag, plus the inertial forces. In contrast, in cases where the sphere moves at an angle to the principal directions of the ambient strain rate, the strain-induced viscous corrections are important and at times outweigh the inertial forces. In such cases, it appears that all three contributions (as included in the third estimate) are necessary for an accurate representation of the total forces.

(*d*) History force: A general expression for the history force, in particular in a non-uniform ambient flow, is likely to be quite complex, and is not the central theme of this paper. Nevertheless, two important observations can be made about the history force from the present results. First, in the context of rapidly imposed straining flows, it is shown that the history kernels of the form (3.21) proposed by Mei & Adrian (1992), which perform very well in a uniform flow, are not adequate to capture the effect of convective acceleration. It is also shown that the history force masks the inertial effect of convective acceleration when a pure straining flow is imposed on a viscously saturated initial flow. In such cases of rapid acceleration, the history force is significant. Therefore, neglecting this force will result in large errors.

However, the rapid acceleration case considered in § 3 is only to isolate the inertial forces over a very short time. In most applications, the acceleration seen by the sphere will not be so rapid, and as a result the history force is not likely to be as high. This is indeed verified by DNS of a freely translating sphere in straining flows. In all the cases considered, for varying ambient strain nature, magnitude and orientation, the total force acting on the sphere over the entire computed period of its free translation can be estimated well without accounting for the history force. This is because for a rigid sphere in free translation in straining flows, the time history of the convective or temporal acceleration seen by the sphere is not strong enough to generate a large history force. Thus, neglecting the history force will not result in a large error in these cases. The inertial forces combined with the correct parameterization for the steady viscous force will provide a reasonable estimate for the exact force on the sphere.

Finally, it should be pointed out that the present paper does not consider the effect of free rotation of the sphere. A freely moving sphere will rotate under the hydrodynamic torque acting on it in addition to its translational motion in response to the hydrodynamic forces. In most of the cases considered here, one of the principal axes of the strain rate aligns with the direction of relative velocity. Due to the symmetry of such cases there is no net hydrodynamic torque on the sphere, and therefore the present simulation of a non-rotating sphere is appropriate. This, however,

is not the case when the sphere moves at an angle to the principal axes of the ambient strain rate. We have performed additional numerical simulations for such cases to consider freely translating and rotating spheres. The results show that over the range of parameters explored here, the free rotation of the sphere has little effect on the forces. Therefore, the conclusions drawn above remain appropriate even when the sphere is allowed to both translate and rotate. Similar observations on the relative insensitivity of the lift and drag forces to free rotation of the sphere have recently been made in the context of linear shear flows (Bagchi & Balachandar 2002*b*).

The research is supported by the ASCI Center for Simulation of Advanced Rockets at the University of Illinois at Urbana-Champaign under the auspices of the US Department of Energy through the University of California subcontract number B341494. Computations are performed on the SGI/CRAY Origin 2000 cluster at the National Center for Supercomputing Applications, UIUC. Special thanks are due to Drs J. P. Ferry and F. M. Najjar. We also acknowledge the referees whose valuable comments have significantly improved the quality of the manuscript.

Appendix. Generalized representation for $\boldsymbol{F}_{\rm sv}$

The parameterization for $\boldsymbol{F}_{\rm sv}$ in pure straining flows was given in § 5. Here we consider the general case of any linear rotational or irrotational ambient flow. Following the representation theorem outlined by Wang (1970) and Smith (1971), $\boldsymbol{F}_{\rm sv}$ can be written as

$$\begin{aligned}\boldsymbol{F}_{\rm sv} = 3\pi d\mu\, g_1\, \boldsymbol{U}_r + m_{\rm f}\, g_2\, \boldsymbol{U}_r \cdot \boldsymbol{S} + \frac{m_{\rm f} d}{|\boldsymbol{U}_r|}\, g_3\, \boldsymbol{U}_r \cdot \boldsymbol{S}^2 \\ + m_{\rm f}\, g_4\, \boldsymbol{U}_r \cdot \Omega + \frac{m_{\rm f} d}{|\boldsymbol{U}_r|}\, g_5\, \boldsymbol{U}_r \cdot \Omega^2 + \frac{m_{\rm f} d}{|\boldsymbol{U}_r|}\, g_6\, \boldsymbol{U}_r \cdot (\boldsymbol{S}\Omega - \Omega \boldsymbol{S}).\end{aligned} \quad \text{(A 1)}$$

The first term on the right corresponds to the Stokes-like drag force. The second and third terms account for additional contributions arising from the strain component of the ambient flow. The fourth and fifth terms similarly account for contributions arising from the rotational component. The last term represents a contribution due to the interaction between the strain and rotational components. The dimensionless quantities g_1, g_2, etc., are functions of a set of isotropic scalar invariants, from $\boldsymbol{U}_r$, $\boldsymbol{S}$ and Ω. The following irreducible list shows all the isotropic scalar invariants arranged in three groups, $G1$, $G2$ and $G3$:

$$\left.\begin{aligned} &G1 : \boldsymbol{U}_r \cdot \boldsymbol{U}_r,\ \mathrm{tr}(\boldsymbol{S}),\ \mathrm{tr}(\boldsymbol{S}^2),\ \mathrm{tr}(\boldsymbol{S}^3),\ \mathrm{tr}(\Omega^2), \\ &G2 : \boldsymbol{U}_r \cdot \boldsymbol{S}\boldsymbol{U}_r,\ \boldsymbol{U}_r \cdot \boldsymbol{S}^2\boldsymbol{U}_r,\ \boldsymbol{U}_r \cdot \Omega^2\boldsymbol{U}_r,\ \mathrm{tr}(\boldsymbol{S}\Omega^2),\ \mathrm{tr}(\boldsymbol{S}^2\Omega^2),\ \mathrm{tr}(\boldsymbol{S}^2\Omega^2\boldsymbol{S}\Omega), \\ &G3 : \boldsymbol{U}_r \cdot \boldsymbol{S}\Omega\boldsymbol{U}_r,\ \boldsymbol{U}_r \cdot \boldsymbol{S}\Omega^2\boldsymbol{U}_r,\ \boldsymbol{U}_r \cdot \Omega\boldsymbol{S}\Omega^2\boldsymbol{U}_r,\ \boldsymbol{U}_r \cdot \boldsymbol{S}^2\Omega\boldsymbol{U}_r. \end{aligned}\right\} \quad \text{(A 2)}$$

The first group accounts for all the fundamental scalar invariants; $\boldsymbol{U}_r \cdot \boldsymbol{U}_r$ measures the magnitude of the relative velocity and $\mathrm{tr}(\Omega^2) = -2|\boldsymbol{\omega}|^2$ measures the rotational rate of the ambient flow, where $\boldsymbol{\omega}$ is the ambient vorticity measured at the centre. In an incompressible fluid $\mathrm{tr}(\boldsymbol{S}) = 0$. The term $\mathrm{tr}(\boldsymbol{S}^2)$ can be interpreted as a measure of the magnitude of strain (s), while $\mathrm{tr}(\boldsymbol{S}^3)$ represents the axisymmetric or planar nature of strain.

The binary scalar invariants, $G2$, are formed by considering $\boldsymbol{U}_r$, $\boldsymbol{S}$ and Ω, two at a time. When appropriately normalized by the fundamental invariants, the binary invariants measure the relative orientation between the relative velocity vector,

principal directions of strain rate and the direction of the vorticity vector. The invariants, $\boldsymbol{U}_r \cdot \boldsymbol{S}\boldsymbol{U}_r$ and $\boldsymbol{U}_r \cdot \boldsymbol{S}^2\boldsymbol{U}_r$, under appropriate normalization can be expressed in terms of the angles Θ and Φ as

$$\frac{\boldsymbol{U}_r \cdot \boldsymbol{S}\boldsymbol{U}_r}{[\boldsymbol{U}_r \cdot \boldsymbol{U}_r][\mathrm{tr}(\boldsymbol{S}^2)]^{1/2}} = \frac{\cos^2\Theta - f_s \sin^2\Theta \cos^2\Phi - (1 - f_s)\sin^2\Theta \sin^2\Phi}{\left[1 + f_s^2 + (1 - f_s)^2\right]}, \quad \text{(A 3)}$$

$$\frac{\boldsymbol{U}_r \cdot \boldsymbol{S}^2\boldsymbol{U}_r}{[\boldsymbol{U}_r \cdot \boldsymbol{U}_r]\mathrm{tr}(\boldsymbol{S}^2)} = \cos^2\Theta + f_s^2 \sin^2\Theta \cos^2\Phi + (1 - f_s)^2 \sin^2\Theta \sin^2\Phi. \quad \text{(A 4)}$$

In a similar way, the invariant $\boldsymbol{U}_r \cdot \Omega^2\boldsymbol{U}_r$, when appropriately normalized, measures the angle between $\boldsymbol{U}_r$ and $\boldsymbol{\omega}$. The next two invariants can be expressed as

$$\mathrm{tr}(\boldsymbol{S}\Omega^2) = \boldsymbol{\omega} \cdot \boldsymbol{S}\boldsymbol{\omega}, \quad \text{(A 5)}$$

$$\mathrm{tr}(\boldsymbol{S}^2\Omega^2) = \boldsymbol{\omega} \cdot \boldsymbol{S}^2\boldsymbol{\omega} - |\boldsymbol{\omega}|^2\mathrm{tr}(\boldsymbol{S}^2). \quad \text{(A 6)}$$

Hence they measure the relative orientation of the vorticity vector with the principal directions of strain.

At first sight it might appear that the configuration formed by the relative velocity vector, $\boldsymbol{U}_r$, the strain-rate and rotation-rate tensors is adequately defined by their magnitudes and relative orientation (or angles between them). The binary invariant, $\mathrm{tr}(\boldsymbol{S}^2\Omega^2\boldsymbol{S}\Omega)$, and the group, $G3$, might appear redundant and therefore seem to be reducible in terms of the other invariants. However, the list provided in (A 2) is irreducible. The physical interpretation of these additional independent scalar invariants is complex. They are important only when both strain and rotation are present. They are required to uniquely characterize the relative orientation of $\boldsymbol{U}_r$, $\boldsymbol{S}$ and Ω. Hence we will not pursue these higher-order invariants and simply refer to the equivalence theorem by Wang (1970).

REFERENCES

Asmolov, E. S. 1999 The inertial lift on a spherical particle in a plane Poiseuille flow at large channel Reynolds number. *J. Fluid Mech.* **381**, 63–87.

Auton, T. R. 1987 The lift force on a spherical body in a rotational flow. *J. Fluid Mech.* **183**, 199–218.

Auton, T. R., Hunt, J. C. R. & Prud'homme, M. 1988 The force exerted on a body in inviscid unsteady non-uniform rotational flow. *J. Fluid Mech.* **197**, 241–257.

Bagchi, P. & Balachandar, S. 2002*a* Steady planar straining flow past a rigid sphere at moderate Reynolds number. *J. Fluid Mech.* **466**, 365–407.

Bagchi, P. & Balachandar, S. 2002*b* Effect of free rotation on the motion of a solid sphere in linear shear flow at moderate *Re*. *Phys. Fluids* **14**, 2719–2737.

Bagchi, P., Ha, M. Y. & Balachandar, S. 2001 Direct numerical simulation of flow and heat transfer from a sphere in uniform cross-flow. *Trans. ASME : J. Fluids Engng* **123**, 347–358.

Batchelor, G. K. 1967 *A Treatise in Hydrodynamics*, vol. 2. Cambridge: Deighton Bell.

Chang, E. J. & Maxey, M. R. 1994 Unsteady flow about a sphere at low to moderate Reynolds number. Part 1. Oscillatory motion. *J. Fluid Mech.* **277**, 347–379.

Chang, E. J. & Maxey, M. R. 1995 Unsteady flow about a sphere at low to moderate Reynolds number. Part 2. Accelerated motion. *J. Fluid Mech.* **303**, 133–153.

Clift, R., Grace, J. R. & Weber, M. E. 1978 *Bubbles, Drops and Particles*. Academic.

Gatignol, R. 1983 The Faxen formulae for a rigid particle in an unsteady non-uniform Stokes flow. *J. Méc. Théor. Applic.* **2**, 143–160.

Herron, I. H., Davis, S. H. & Bretherton, F. P. 1975 On the sedimentation of a sphere in a centrifuge. *J. Fluid Mech.* **68**, 209–234.

Howe, M. S. 1995 On the force and moment on a body in an incompressible fluid, with application to rigid bodies and bubbles at low and high Reynolds numbers. *Q. J. Mech. Appl. Maths* **48**, 401–426.

Kim, I., Elghobashi, S. & Sirignano, W. A. 1998 On the equation for spherical-particle motion: effect of Reynolds and acceleration numbers. *J. Fluid Mech.* **367**, 221–254.

Lamb, H. 1932 *Hydrodynamics*, 6th edn. Cambridge University Press.

Lovalenti, P. M. & Brady, J. F. 1993 The force on sphere in a uniform flow with small-amplitude oscillations at finite Reynolds number. *J. Fluid Mech.* **256**, 607–614.

Magnaudet, J. 1997 The forces acting on bubbles and rigid particles. *ASME Fluids Engng Summer Meeting*. FEDSM 97-3522.

Magnaudet, J. & Eames, I. 2000 The motion of high-Reynolds-number bubbles in inhomogeneous flows. *Annu. Rev. Fluid Mech.* **32**, 659–708.

Magnaudet, J., Rivero, M. & Fabre, J. 1995 Accelerated flows past a rigid sphere or a spherical bubble. Part 1. Steady straining flow. *J. Fluid Mech.* **284**, 97–135.

Maxey, M. R. & Riley, J. J. 1983 Equation of motion for a small sphere in a non-uniform flow. *Phys. Fluids* **26**, 883–889.

McLaughlin, J. B. 1991 Inertial migration of a small sphere in linear shear flows. *J. Fluid Mech.* **224**, 261–274.

McLaughlin, J. B. 1993 The lift on a small sphere in wall-bounded linear shear flows. *J. Fluid Mech.* **246**, 249–265.

Mei, R. 1994 Flow due to an oscillating sphere and an expression for unsteady drag on the sphere at finite Reynolds number. *J. Fluid Mech.* **270**, 133–174.

Mei, R. & Adrian, R. J. 1992 Flow past a sphere with an oscillation in the free-stream and unsteady drag at finite Reynolds number. *J. Fluid Mech.* **237**, 323–341.

Mei, R., Lawrence, C. J. & Adrian, R. J. 1991 Unsteady drag on a sphere at finite Reynolds number with small fluctuations in the free-stream velocity. *J. Fluid Mech.* **233**, 613–631.

Miyazaki, K., Bedeaux, D. & Avalos, J. B. 1995 Drag on a sphere in slow shear flow. *J. Fluid Mech.* **296**, 373–390.

Mittal, R. & Balachandar, S. 1996 Direct numerical simulation of flow past elliptic cylinders. *J. Comput. Phys.* **124**, 351-367.

Mougin, G. & Magnaudet, J. 2001 The generalized Kirchhoff equations and their application to the interaction between a rigid body and an arbitrary time-dependent viscous flow. *Intl J. Multiphase Flow* (to appear).

Pérez-Madrid, A., Rubí, J. M. & Bedeaux, D. 1990 Motion of a sphere through a fluid in stationary homogeneous flow. *Physica* A **163**, 778–790.

Rivero, M., Magnaudet, J. & Fabre, J. 1991 Quelques resultats nouveaux concernant les forces exercees sur une inclusion spherique par un ecoulement accelere. *C. R. Acad. Sci. Paris* **312**, II, 149–1506.

Saffman, P. G. 1965 The lift on a small sphere in a slow shear flow. *J. Fluid Mech.* **22**, 385–400 (and Corrigendum, 1968, **31**, 624).

Schiller, L. & Neumann, A. 1933 Uber die grundlegenden Berechungen bei der Schwerkraftaufbereitung. *Ver. Deutt. Ing.* **77**, 318.

Smith, G. F. 1971 On isotropic functions of symmetric tensors, skew-symmetric tensors and vectors. *Intl J. Engng Sci.* **9**, 899–916.

Sridhar, G. & Katz, J. 1995 Drag and lift forces on microscopic bubbles entrained by a vortex. *Phys. Fluids* **7**, 389–399.

Taylor, G. I. 1928 The forces on a body placed in a curved or converging stream of fluid. *Proc. R. Soc. Lond.* A **120**, 260.

Tchen, C. M. 1947 Mean value and correlation problems connected with the motion of small particles suspended in a turbulent fluid. PhD Dissertation, Technische Hogeschool Delft.

Tollmien, W. 1938 Uber krafte und momente in schwach gekrummten oder konvergenten stromungen. *Ing.-Arch.* **9**, 308.

Voinov, V. V., Voinov, O. V. & Petrov, A. G. 1973 Hydrodynamic interactions between bodies in a perfect incompressible fluid and their motion in non-uniform streams. *Prikl. Math. Mekh.* **37**, 680.

Wang, C. C. 1970 A new representation theorem for isotropic functions. *Arch. Rat. Mech. Anal.* **36**, 166–197.